Inorganic Chemistry
Article
pubs.acs.org/IC

Electronic Structure and Spectroscopic Properties of Mononuclear Manganese(III) Schiff Base Complexes: A Systematic Study on [Mn(*acen*)X] Complexes by EPR, UV/vis, and MCD Spectroscopy (X = Hal, *NCS*)

Anne Westphal, Arne Klinkebiel, Hans-Martin Berends, Henning Broda, Philipp Kurz, and Felix Tuczek*

Institut für Anorganische Chemie, Christian-Albrechts-Universität zu Kiel, D-24118 Kiel, Germany

Supporting Information

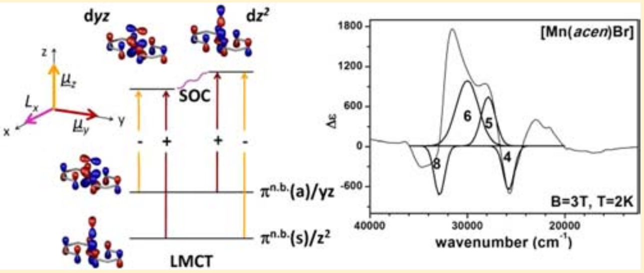

ABSTRACT: The manganese(III) Schiff base complexes [Mn(*acen*)X] (*H_2acen*: *N*,*N*′-ethylenebis(acetylacetone)imine, X: I^-, Br^-, Cl^-, *NCS^-*) are considered as model systems for a combined study of the electronic structure using vibrational, UV/vis absorption, parallel-mode electron paramagnetic resonance (EPR) and low-temperature magnetic circular dichroism (MCD) spectroscopy. By variation of the co-ligand X, the influence of the axial ligand field within a given square-pyramidal coordination geometry on the UV/vis, EPR, and MCD spectra of the title compounds is investigated. Between 25000 and 35000 cm^{-1}, the low-temperature MCD spectra are dominated by two very intense, oppositely signed *pseudo-A* terms, referred to as "double *pseudo-A* terms", which change their signs within the [Mn(*acen*)X] series dependent on the axial ligand X. Based on molecular orbital (MO) and symmetry considerations, these features are assigned to $\pi^{n.b.}(s, a) \rightarrow yz, z^2$ ligand-to-metal charge transfer transitions. The individual MCD signs are directly determined from the calculated MOs of the [Mn(*acen*)X] complexes. The observed sign change is explained by an inversion of symmetry among the $\pi^{n.b.}(s, a)$ donor orbitals which leads to an interchange of the positive and negative *pseudo-A* terms constituting the "double *pseudo-A* term".

■ INTRODUCTION

Some of the most important biological redox processes are catalyzed by manganese metalloenzymes. Manganese containing superoxide dismutase (MnSOD) and catalase (MnCat), for example, protect cells from oxidative damage by catalyzing the decomposition of superoxide and hydrogen peroxide. Both reactions involve electron transfer mediated by mono- and dinuclear manganese centers within the active sites of MnSOD (one-electron transfer) and MnCat (two-electron transfer), respectively.[1−5] Moreover, the photosynthetic water oxidation, which is one of the most fundamental redox reactions in vivo, is catalyzed by a Mn_4CaO_5 cluster located in the *oxygen-evolving complex* (OEC) at the luminal side of the photosystem II in the thylakoid membrane of phototrophic plants, algae, and cyanobacteria. It consists of a tetranuclear manganese unit[6−8] and is able to catalyze the light-induced water splitting in four successive one-electron steps.[9−13]

Inspired by MnSOD, MnCat, and the OEC of photosystem II, numerous complexes have already been designed and studied as structural, spectroscopic, and mechanistic biomimetic models of the natural enzymes.[14−20] Of fundamental interest with respect to these systems is the characterization of their electronic properties, that is, oxidation and spin states, redox potentials and magnetic couplings (if di- and polynuclear manganese complexes are involved), to understand their reactivities and those of their biological counterparts. A very useful and well-established technique in this regard is electron paramagnetic resonance (EPR) spectroscopy. In particular, reactive intermediates of (catalytic) redox reactions can be detected and characterized by this method.[21−38] Different oxidation and spin states can be distinguished, and specific parameters like *g*-values, zero-field splitting parameters, and coupling constants can be determined. Unfortunately, EPR is only limited to paramagnetic systems, so antiferromagnetically coupled manganese centers like Mn(III,III) or Mn(IV,IV) dimers cannot be detected or analyzed as they are EPR silent.

Another powerful tool to gain insight into the electronic structure of transition metal complexes is magnetic circular dichroism (MCD) spectroscopy.[39−55] In contrast to conventional UV/vis absorption spectra, the corresponding MCD spectra contain more detailed information about the electronic states of the considered metal ion(s). In MCD spectroscopy, the differential absorption $\Delta\varepsilon$ between left (lcp) and right (rcp) circular polarized light of a sample is measured in the presence of a longitudinal magnetic field. As $\Delta\varepsilon$ can be positive or negative, the observed MCD transitions exhibit positive or negative signs. This potentially renders MCD spectroscopy superior to ordinary electronic absorption spectroscopy where only (intrinsically positive) absorption intensities are recorded.

Received: August 29, 2012
Published: February 14, 2013

dx.doi.org/10.1021/ic301889e | *Inorg. Chem.* 2013, 52, 2372−2387

Moreover, the magnetic-field and temperature dependence (see below) allows to employ MCD spectroscopy for the determination of electronic ground-state properties; that is, *g*- and *D*-tensors. While the latter application (which is complementary to EPR) is well established,[39,43,45,46,52,56,57] it is still a difficult task to extract the information content present in MCD spectra with respect to the manifold of excited states. The current paper is therefore mainly concerned with the excited states of the [Mn(*acen*)X] complexes and the absolute signs of the observed MCD transitions, and how they can be extracted from a calculated MO scheme.

Three different mechanisms give rise to an MCD signal which are designated as *A*-, *B*-, and *C*-term intensity.[58,59] While *A*-term intensity arises from the splitting of an orbitally degenerate excited state in the presence of an external magnetic field and shows a derivative band shape, *C*-term intensity is observed as a consequence of the splitting of a degenerate ground state. A third contribution, *B*-term intensity, arises from the coupling of two formerly independent excited states in the presence of an external magnetic field. Like the MCD *C*-term mechanism, it gives rise to a usual absorption band shape. In contrast to the *A*- and *B*-term intensities, the MCD *C*-term intensity is temperature dependent ($\sim 1/T$) and dominates the MCD spectra at very low temperatures. In the limit of a pure *C*-term mechanism, the MCD intensity is given by

$$\frac{\Delta\varepsilon}{E} = \frac{\varepsilon_{\mathrm{lcp}} - \varepsilon_{\mathrm{rcp}}}{E} = \frac{\gamma\beta_{\mathrm{B}}B}{kT}\bar{C}_0\, f(E)$$

where γ is a collection of constants, β_{B} is the Bohr magneton, k is the Boltzmann constant, T is the absolute temperature, B is the magnetic flux density, $f(E)$ is a line shape function, and $\bar{C}_0$ contains the effective transition dipole moments (see below). Here, it is sufficient to consider $f(E)$ as a δ-function and E as the transition energy. In the saturation limit of very low temperatures and very high fields, the MCD *C*-term intensity results as[35]

$$\frac{\Delta\varepsilon}{E} = -\frac{1}{3}\gamma(M_{yz}^{\mathrm{eff}} + M_{zx}^{\mathrm{eff}} + M_{xy}^{\mathrm{eff}})$$

where $M_{vw}{}^{\mathrm{eff}}$ are effective transition dipole moments ($vw = xy$, xz, and yz) which are given by

$$M_{vw}^{\mathrm{eff}} = \sum_{K\neq A,J}\left\{(\vec{D}_v^{AK}\vec{D}_w^{AJ} - \vec{D}_w^{AK}\vec{D}_v^{AJ})\frac{\bar{L}_u^{KJ}}{\Delta_{KJ}} + (\vec{D}_v^{AJ}\vec{D}_w^{JK} - \vec{D}_w^{AJ}\vec{D}_v^{JK})\frac{\bar{L}_u^{KA}}{\Delta_{KA}}\right\}$$

The states A, J, and K all have the same spin multiplicity and are given as eigenfunctions of S and S_Z; that is, $A = |ASM_S\rangle$ and so forth (u, v, $w = x$, y, z). The transition dipole matrix elements $\vec{D}_u^{AB}$ are defined as

$$\vec{D}_u^{AB} = \langle ASM_S|\mu_u|BSM_S\rangle$$

and the reduced spin–orbit coupling matrix elements $\bar{L}_u^{AB}$ are defined as

$$\bar{L}_u^{AB} = \mathrm{Im}\langle ASS|\sum_i h_u(i)\; s_0(i)|BSS\rangle_0$$

where $s_0(i)$ is the s_z component of the spin operator acting on the ith electron and the sum runs over all electrons i. In this expression, the operator $h_u(i)$ is given by

$$h_u(i) = \sum_N \xi(r_{iN})l_{N,u}(i)$$

where N denotes the atom and ξ is the spin–orbit coupling constant. $l_{N,u}(i)$ is the u-th component of the orbital-angular momentum operator acting on electron i relative to nucleus N. Spin–orbit coupling is usually only considered within the metal atom.[39]

The above equations indicate that MCD *C*-term intensity may arise through spin–orbit coupling between the excited states J and K ($A \to J$, $A \to K$, J and K being coupled through spin–orbit coupling; "*J*-*K* coupling") or between the ground state A and an excited state K ($A \to J$, $K \to J$, A and K being coupled through spin–orbit coupling; "*A*-*K* coupling"). Considering the "*J*-*K* coupling" mechanism, the individual transitions, $A \to J$ and $A \to K$, must be polarized in different directions perpendicular to the angular momentum vector between J and K to result into nonzero *C*-term intensities (Scheme 1, left).[39] If both transitions are observed in the MCD spectra, they show opposite signs and, if the excited state splitting $\Delta_{KJ} = E_K - E_J$ is comparable to the bandwidth, may appear as one derivative-shaped band which is then called a *pseudo-A* term. The absolute signs of the $A \to J$ and $A \to K$ transitions generally depend on the symmetry of the considered states; that is, on the symmetry of the involved molecular orbitals.

Scheme 1

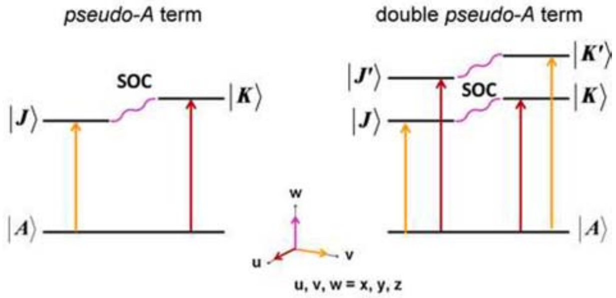

Four MCD transitions, $A \to J$, $A \to K$ and $A \to J'$ and $A \to K'$, arising from *C*-term transitions between a pair of (almost) degenerate donor orbitals and a pair of (almost) degenerate acceptor orbitals of appropriate symmetry may be observed as two oppositely signed *pseudo-A* terms of equal intensity which is then called a "double *pseudo-A* term" (Scheme 1, right).[60] Consisting of four related MCD bands, this spectral feature shows a characteristic pattern of positive-negative-negative-positive or negative-positive-positive-negative intensities, depending on the particular symmetries of the involved orbitals.

A general quantum-mechanical formalism to calculate the signs and intensities of MCD *C*-term transitions for spins $\geq 1/2$ has previously been presented by Neese and Solomon.[39] Some rare examples concerning the theoretical calculation of MCD signs and intensities have also been reported so far.[61−64] Additionally, we recently published a detailed analysis of the MCD signs and intensities of the "double *pseudo-A* term" transitions observed in the MCD spectrum of the Mo(V) complex [MoCl$_3$(*dppe*)] (*dppe*: 1,2-bis(diphenylphosphino)-ethane).[60] In general, however, the direct assignment of MCD transitions based on the direct determination of the MCD signs and intensities is still nonstandard. In consequence, the MCD spectra of MnSOD, MnCat, and some mono- and dinuclear

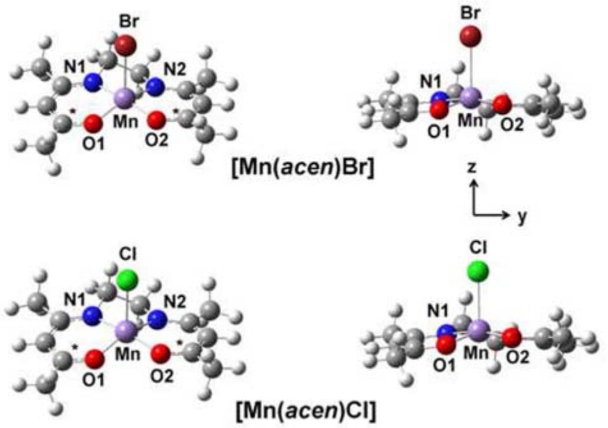

Figure 1. DFT geometry optimized complex structures of [Mn(*acen*)Br] and [Mn(*acen*)Cl] (B3LYP/LANL2DZ). The coordinating *acen* N and O atoms are not coplanar (right).

manganese complexes, which have already been described in the literature, were mainly analyzed without accounting for the particular signs of the observed *C*-term transitions. In most cases, the reported assignments were based on indirect methods, for example, geometry considerations, resonance Raman investigations, and (time dependent) density functional theory calculations of molecular orbitals and electronic transitions.[20,48−55]

This being the situation, we intended to study the MCD spectra of Mn complexes to systematically analyze and understand the origin of the positive and negative signs of the observed transitions. We started with the analysis of the MCD spectra of very simple *mono*nuclear manganese(III) complexes and herein present a study on the UV/vis and MCD spectra of a the series of [Mn(*acen*)X] complexes ($X^- = I^-$, Br^-, Cl^-, NCS^-), well-known representatives of five-coordinate, square-pyramidal Mn(III) complexes containing the aliphatic Schiff base ligand $acen^{2-}$ (H_2acen: *N,N′*-ethylenebis(acetylacetone)imine).[65] First of all, the [Mn(*acen*)X] complexes were thoroughly characterized by vibrational spectroscopy. Additionally, the low-temperature parallel mode EPR spectra were studied in detail. Then we analyzed the UV/vis and MCD spectra of the different [Mn(*acen*)X] compounds. The assignment of the MCD spectra and the determination of the individual MCD signs were based on molecular orbital (MO) calculations and symmetry considerations, following a procedure which was originally described by Neese and Solomon and previously applied to the analysis of the MCD spectrum of $[MoCl_3(dppe)]$.[39,60] The molecular orbitals of the [Mn(*acen*)X] complexes were computed with density functional theory (DFT). This way, we were also able to study the influence of a varying ligand field strength ($I^- < Br^- < Cl^- < NCS^-$) within a given square-pyramidal coordination geometry on the EPR, UV/vis, and MCD spectra of the [Mn(*acen*)X] complexes and in particular interpret the sign change of the “double *pseudo-A* terms” observed in the MCD spectra as a function of X.

■ EXPERIMENTAL SECTION

Synthesis. The H_2acen ligand was prepared by the condensation of ethylene diamine and 2 equiv of acetyl acetonate[66] and recrystallized from water. The synthesis of the [Mn(*acen*)X] complexes was done according to literature procedures[65] achieving good yields and high purity which was checked by elemental analysis and atomic absorption spectroscopy (Supporting Information, Table S1).

Vibrational Spectroscopy. MIR spectra of the solid samples were measured in KBr between 400 cm^{-1} and 4000 cm^{-1} using a Bruker IFS v66/S FT-IR spectrometer. Far infrared (FIR) spectra were recorded between 100 cm^{-1} and 550 cm^{-1} using a Bruker IFS 66 FIR spectrometer. The solid compounds were lubricated with silicon and halogen free grease (Apiezon) between thin PE sheets. The FT-Raman spectra of the solid samples were recorded with a Bruker IFS 666/CS NIR FT-Raman spectrometer. A Nd:YAG laser with an excitation wavelength of 1 064 nm was used as a light source. The analysis of the vibrational spectra is presented in the Supporting Information, Figure S1, Table S2.

Parallel Mode cw X-band EPR Spectra. Low-temperature parallel mode cw X-band EPR spectra were collected at temperatures between 4 and 25 K using a Bruker EMX*plus* spectrometer with a PremiumX microwave bridge equipped with an Oxford Instrument ESR 900 cryostat, an Oxford ITC-4 temperature controller, and a dual mode cavity (Bruker ER-4116DM). Samples were prepared as frozen CH_2Cl_2/toluene (7:3) and MeOH solutions of different concentrations (1 mM−10 mM, 200 μL) in 1 mm quartz tubes. Resonance in the perpendicular detection mode was also checked for each sample to exclude that manganese(II) or -(VI) species were present at the same time. EPR data collection was managed using the Bruker Xenon 1.0 software package. Spectral simulations were performed using the EPR simulation software package EasySpin.[67]

UV/vis Absorption Spectroscopy. UV/vis spectra of 2 mM complex solutions in CH_2Cl_2 as well as of thin polystyrene films used for the MCD measurements (vide infra) were recorded at room temperature using a Cary 5000 NIR spectrophotometer (Varian) at wavelengths between 1500 and 200 nm. Low-temperature UV/vis spectra of the polystyrene film samples were recorded at 100 K using a KONTI cryostat associated with a TIC-300 MA temperature controller (CryoVac).

Magnetic Circular Dichroism Measurements. Low-temperature MCD spectra were recorded using a JASCO J810 CD spectropolarimeter associated with an OXFORD SM 4000-9 magnetocryostat at temperatures around 2 K and magnetic field strengths between 0 and (up to) ±7 T as previously described.[45] Samples were prepared as thin polystyrene films by the evaporation of 1 mM complex solutions in CH_2Cl_2 containing a sufficient amount of dissolved polystyrene. Using two interchangeable head-on photomultiplier tubes, MCD spectra for a combined wavelength range of 200−1100 nm (50000−9000 cm^{-1}) could be recorded. After the subtraction of the $B = 0$ T reference spectrum, the resulting MCD spectra were deconvoluted by Gaussian curve fits to resolve the individual transitions.

Density Functional Theory (DFT) Computations. Spin-unrestricted DFT calculations were performed with Gaussian03[68] using the B3LYP hybrid functional.[69−71] The LANL2DZ basis set was used for all types of atoms for the geometry optimization of the complex structures and the calculation of the vibrational spectra.[72−75] The molecular orbitals were calculated using Ahlrich’s def2tzvp basis set as obtained from the Basis-Set Exchange homepage EMSL for all types of atoms.[76−78] The molecular orbitals were plotted with Gabedit.[79]

■ RESULTS AND DISCUSSION

DFT Optimized Complex Structures. From the DFT geometry optimizations of the [Mn(*acen*)X] complexes square-pyramidal coordination geometries of pseudo-C_S symmetry were obtained. This is shown in Figure 1 for the chlorido and bromido complexes, [Mn(*acen*)Cl] and [Mn(*acen*)Br].

The increasing ligand field strength of the axial ligand X ($I^- < Br^- < Cl^- < NCS^-$) is very well reproduced by the decreasing Mn−X metal−ligand bond lengths (ranging from 2.85 Å for the iodido complex to 2.04 Å for the *NCS* complex) as well as by the increasing axial displacement of the Mn(III) ion which is

Table 1. Overview of the Most Important Structural Parameters of the [Mn(*acen*)X] Complexes Extracted from DFT Optimized Complex Geometries (B3LYP/LANL2DZ)

	Mn−X [Å]	Mn−N1/N2 [Å]	Mn−O1/O2 [Å]	N1−O2−Mn	Mn displacement[a]	*acen* twist[b]
[Mn(*acen*)I]	2.85	1.97/2.00	1.91/1.89	5.9°	0.19 Å	−9.2°
[Mn(*acen*)Br]	2.62	1.97/2.00	1.91/1.89	6.5°	0.21 Å	−8.8°
[Mn(*acen*)Cl]	2.43	1.97/2.01	1.92/1.90	6.7°	0.22 Å	−9.5°
(X-ray structure)[65]	(2.38)	(1.97)	(1.90)		(0.34 Å)	
[Mn(*acen*)NCS]	2.04	1.98/2.01	1.93/1.90	7.3°	0.24 Å	−8.5°

[a] The axial displacement b of the manganese ion is determined by $b = \sin(\text{N1−O2−Mn angle})\cdot\text{Mn−O2 distance}$. [b] O1−N1−N2−O2 dihedral angle.

lifted from the equatorial plane (xy) in the positive z direction by 0.19 Å in the case of [Mn(*acen*)I] and up to 0.24 Å in the case of [Mn(*acen*)NCS] (Table 1). As the two arms of the *acen*$^{2-}$ Schiff base ligand are twisted by about 9° (O1−N1−N2−O2 dihedral angle), the coordinating N and O atoms are not coplanar. The Mn−O and Mn−N metal−ligand bond distances, however, do not vary within the [Mn(*acen*)X] series.

In the case of the chlorido complex, the calculated complex structure can be compared to structural data which had been obtained from a single crystal X-ray analysis and were reported by Boucher and Day.[65] The calculated Mn−O/N distances perfectly match the averaged Mn−O (1.90 Å) and Mn−N (1.97 Å) bond lengths observed within the crystal structure. In contrast, the calculated Mn−Cl distance of 2.43 Å is elongated compared to the crystal structure (2.38 Å), and the axial displacement of the Mn(III) ion toward the axial chlorido ligand is found to be smaller in the calculated structure (0.22 Å) than in the crystal structure (0.34 Å). In the single crystal X-ray structure, the four coordinating *acen* N and O atoms are almost coplanar, and the backbones of the two acetylacetone imine side arms of the *acen* ligand are bent toward the unoccupied coordination site of the Mn(III) ion by 14.9° and 18.6°.[65] Actually, this is the most remarkable difference compared to the DFT geometry optimized complex structure, where a twisted conformation of the *acen*$^{2-}$ ligand is obtained with the four coordinating N and O atoms not being coplanar (vide supra). The latter also applies to the calculated structures of the iodido, bromido, and *N*CS complexes.

To make sure that the DFT optimized complex structures can nonetheless be used for the theoretical calculation of the molecular orbitals, the experimental and calculated infrared (IR) and Raman spectra of the [Mn(*acen*)X] complexes were analyzed. The detailed assignment of the vibrational spectra of the bromido complex is presented in the Supporting Information, Figure S1, Table S2. The very good match between the experimental and the calculated IR and Raman spectra assures the reliability of the optimized complex structures for their further use in the molecular-orbital calculations (vide infra).

Electron Paramagnetic Resonance. Low-temperature EPR spectra of 2 mM frozen complex solutions were recorded to make sure that the [Mn(*acen*)X] complexes are present as mononuclear Mn(III) species in solution indeed. In the parallel mode cw X-band EPR spectra of the [Mn(*acen*)X] complexes one signal was detected arising from the $|-2\rangle \rightarrow |+2\rangle$ transition of an $S = 2$ system with a large axial zero-field splitting value of $|D| > 0.3$ cm^{-1} (Figure 2).[28,31,80] A hyperfine splitting of $A \approx 42$ G is observed for all [Mn(*acen*)X] compounds. It originates from the coupling of the M_S sublevels with the nuclear spin I of 5/2 for ^{55}Mn and, based on the selection rule of $\Delta I = 0$, leads to the observed sextet which is characteristic for a mononuclear Mn(III) species in a well-defined molecular coordination geometry.[28,30,31,38]

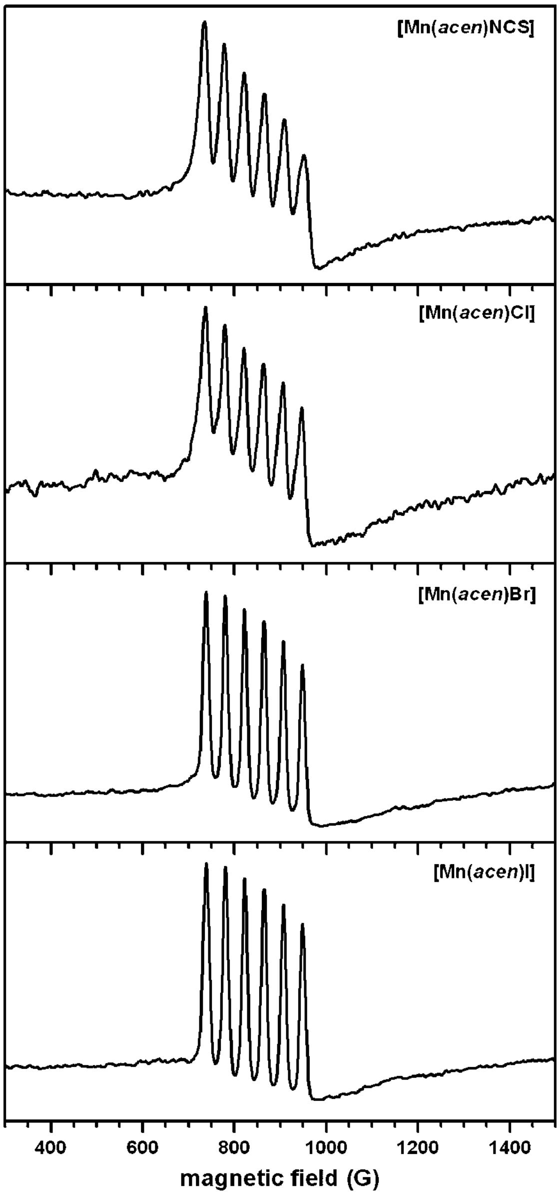

Figure 2. Low-temperature parallel mode cw X-band EPR spectra of [Mn(*acen*)X] measured in frozen CH_2Cl_2/toluene solutions (7:3, 2 mM) at $T = 5$ K (microwave power 2 mW, modulation frequency 100 kHz, modulation amplitude 10 G).

In contrast to a previous study on the parallel mode EPR spectra of the related [Mn(*salen**)Cl] complex (Jacobsen's epoxidation catalyst, *salen** = (*R*,*R*)-(-)-*N*,*N*′-bis(3,5-di-*tert*-butylsalicylidene)-1,2-cyclo-hexaneimine)[31] these well-resolved sextets could be detected without using coordinating additives like *N*-methylmorpholine-*N*-oxide or 4-phenylpyridine-*N*-oxide. In consequence, the presence of dimers, chains, or aggregates can be ruled out in the case of the [Mn(*acen*)X] complexes at the used concentrations of 2 mM. However, at higher concentrations (≥5 mM) the parallel mode EPR spectra of the [Mn(*acen*)X] complexes show additional lines which can be compared to the EPR spectra of [Mn(*salen**)Cl] *without* additives[31] (Supporting Information, Figure S2) and therefore suggest that μ-carboxido- or μ-halogenido-bridged dimers, $[\mathrm{Mn}(acen)\mathrm{X}]_x$ clusters, chains, or other di- and polynuclear species may be formed at high concentrations.[81−83]

At higher temperatures, the parallel mode EPR signals of the [Mn(*acen*)X] complexes linearly decrease with T^{-1}, as expected from Curie's Law. This was also observed for the [Mn(*salen**)-Cl] complex as well as for a Mn(III) species which was obtained by photooxidation of a Mn(II) ion of the photosystem II. In both cases, D was assumed to be negative (−2.5 cm^{-1}).[30,31] In contrast, a nonlinear temperature dependence of the low-temperature parallel mode EPR spectra has been described for MnSOD where a positive zero-field splitting parameter of $D = +2.1\ \mathrm{cm}^{-1}$ has been obtained.[28,38] A power study of the parallel mode EPR signal of [Mn(*acen*)Cl] and the temperature-dependent EPR measurements of the [Mn(*acen*)-X] complexes are presented in the Supporting Information, Figure S3 and S4.

From spectral simulations performed with the simulation software package EasySpin[67] the parallel hyperfine tensor and *g*-matrix values ($A_{\parallel}$, $g_{\parallel}$) as well as the axial and rhombic zero-field splitting parameters D and E were obtained. (Figure 3 and Supporting Information, Figures S5−S7). As expected, they do not vary much throughout the [Mn(*acen*)X] series (Supporting Information, Table S3). Note that, in general, $A_{\perp}$ and $g_{\perp}$ cannot be obtained from parallel mode EPR measurements, so that spectral simulations are not sensitive to the variation of these two parameters. The sign of the zero-field splitting parameters D and E also cannot be obtained directly from the spectral simulations. D, however, is assumed to be negative for the [Mn(*acen*)X] complexes.[30,31] A best fit of the parallel mode EPR spectrum of [Mn(*acen*)Cl] has been obtained with $g_{\parallel} = 1.99$, $A_{\parallel} = 39.1 \times 10^{-4}\ \mathrm{cm}^{-1}$, $D = -2.9\ \mathrm{cm}^{-1}$, and $|E| = 0.16\ \mathrm{cm}^{-1}$ ($g_{\perp} = 2.04$, $A_{\perp} = 99.9 \times 10^{-4}\ \mathrm{cm}^{-1}$). The spectral simulations for the other three complexes are given in the Supporting Information, Figures S5−S7. All parameters are within the typical ranges for mononuclear Mn(III) compounds exhibiting square-pyramidal or tetragonal complex geometries.[30,31] For trigonal-bipyramidal coordination as it is present in MnSOD, a much larger hyperfine coupling of $A_{\parallel} \approx 100$ G is observed.[28,38]

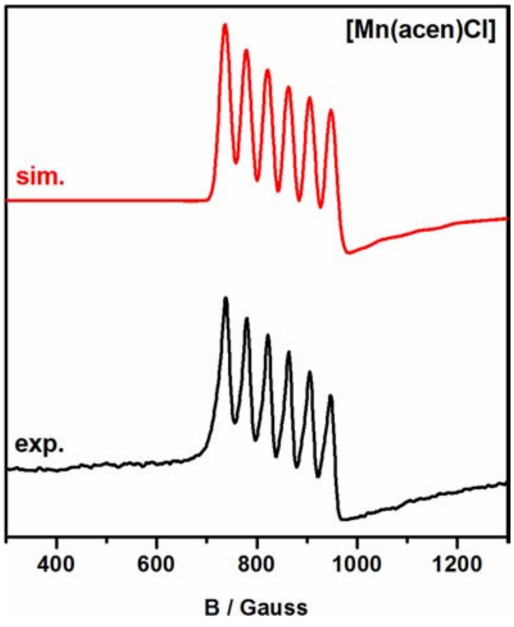

Figure 3. Parallel mode cw X-band EPR spectra of [Mn(*acen*)Cl] measured in a frozen $\mathrm{CH_2Cl_2}$/toluene solution (7:3, 2 mM) at $T = 5$ K (microwave power 2 mW, modulation frequency 100 kHz, modulation amplitude 10 G) and spectral simulation: $g_{\parallel} = 1.99$, $A_{\parallel} = 39.1 \times 10^{-4}$ cm^{-1}, $D = -2.9\ \mathrm{cm}^{-1}$, and $|E| = 0.16\ \mathrm{cm}^{-1}$, ($g_{\perp} = 2.04$, $A_{\perp} = 99.9 \times 10^{-4}\ \mathrm{cm}^{-1}$, line width: 25 G).

As can be seen in Figure 3, two different line widths are observed for the different [Mn(*acen*)X] compounds, as the hyperfine lines of [Mn(*acen*)I] and [Mn(*acen*)Br] appear much sharper (14 G) than those of [Mn(*acen*)Cl] and [Mn(*acen*)-NCS] (20−25 G). This could probably be explained by small monomer−dimer equilibria which can be neglected for the iodido and bromido complexes, but lead to the presence of very small amounts of dimers and/or polymers in the case of the chlorido and the *NCS* complex. Another argument in favor of this explanation is that the same narrow line width of approximately 14 G is detected for all [Mn(*acen*)X] complexes in coordinating solvents like MeOH (Supporting Information, Figure S8) suggesting that the solvent molecules may occupy the free axial positions of the metal ions, so that only discrete mononuclear Mn(III) species are present then.

Considering the results of the low-temperature parallel-mode EPR measurements, it can be concluded that the variation of the axial ligand X virtually has no effect on the EPR spectra. However, they allowed to characterize the $S = 2$ ground state of the [Mn(*acen*)X] complexes. Moreover, it became clear that only concentrations up to 2 mM should be used for any spectroscopic measurements, as higher concentrations probably lead to the formation of undefined polymeric species in solution.

UV/Visible Absorption and MCD Spectra. The d-orbitals of a five-coordinate transition metal ion in a square-pyramidal coordination geometry generally split into one degenerate (d*xz*, d*yz*) and three nondegenerate sublevels ($\mathrm{d}x^2{-}y^2$, $\mathrm{d}z^2$, and d*xy*). Note that in the case of the [Mn(*acen*)X] complexes the *x*- and *y*-axes are assumed to bisect the metal−ligand angles of the equatorial plane (Figure 1). Within the d^4 high-spin configuration of Mn(III), the d*xy* orbital is then unoccupied, leading to a $^5\mathrm{B}_2$ ground state and three metal-centered excited states (Scheme 2).[65] In consequence, three ligand field transitions are expected in the UV/vis absorption spectra of

Scheme 2

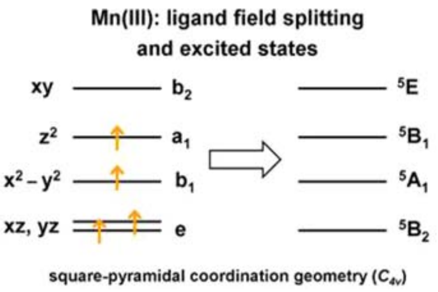

the [Mn(*acen*)X] complexes. Additionally, ligand-to-metal charge transfer (LMCT) from the p-orbitals of the axial ligand and the *acen* π-orbitals into the Mn d-orbitals as well as metal-to-ligand charge transfer (MLCT) into the π^* orbitals of the *acen* ligand have to be considered.

Upon variation of the axial ligand X, no significant differences are observed in the UV/vis absorption spectra of the [Mn(*acen*)X] complexes with respect to the energies and the intensities of the observed transitions (Figure 4, top). An assignment of the UV/vis spectra has already been proposed by Boucher and Day.[65] According to their work, the first spin-allowed ligand field transition ($^5B_2 \rightarrow {}^5A_1$) would be expected at energies below 8000 cm^{-1} but has not been observed so far for any [Mn(*acen*)X] compound. In contrast, the $^5B_2 \rightarrow {}^5B_1$ transition is observed as a broad, low-intensity band at 16400 cm^{-1} (band A, ε = 200 L mol^{-1} cm^{-1}). The $^5B_2 \rightarrow {}^5E$ transition is expected around 20500 cm^{-1}, but is superimposed by a more intense charge transfer transition centered at 22300 cm^{-1} (ε = 1600−1900 L mol^{-1} cm^{-1}). This band has been assigned to the dx^2−y^2 → π^* MLCT transition by Boucher and Day for the reason that no energetic shift of this band is observed on the exchange of the axial ligand.[65] From the UV/vis spectrum of the iodido complex, however, it can be assumed that it actually consists of (at least) two transitions centered at 21200 cm^{-1} and 23500 cm^{-1} (Figure 4 (top), band B and C).

Another charge transfer transition is observed at 25000−27000 cm^{-1} (ε = 5500−7500 L mol^{-1} cm^{-1}, band D). This band is slightly affected by the exchange of the axial ligand X and therefore has been assigned to the d*xz*, d*yz* → π^* MLCT transitions by Boucher and Day.[65] The splitting of band D was explained by the splitting of the ^5E state in distorted square-pyramidal coordination geometries where the degeneracy of the d*xz* and d*yz* orbitals is removed. Using coordinating solvents like methanol, ethanol, or water/glycerol, this absorption band shifts to higher energies by about 2000 cm^{-1}. The blue shift is also associated with an increased absorbance (Supporting Information, Figure S9) which also implies that the orbitals involved in these transitions are noticeably affected by the change of coordination in the axial positions of the Mn(III) ion.

Additionally, a large "plateau" is observed at around 30500 cm^{-1} in the UV/vis absorption spectra of [Mn(*acen*)Br] and [Mn(*acen*)Cl]. This indicates the presence of another absorption band E which has not been described in the literature so far, but is confirmed by the low-temperature UV/vis spectrum of [Mn(*acen*)Cl]. Here, band E is centered at around 30800 cm^{-1} (Supporting Information, Figure S11).

In the UV/vis spectrum of [Mn(*acen*)I], the splitting of band D at around 26000 cm^{-1} as well as the presence of an additional absorption band E around 30000 cm^{-1} are not very well resolved. In the case of [Mn(*acen*)NCS], the splitting of band D, however, is clearly resolved but shows an inverse intensity ratio compared to the halogenido complexes. Additionally, another absorption shoulder is identified at 28500 cm^{-1} in the UV/vis spectrum of the *N*CS complex.

Band F, which is observed at 33500 cm^{-1} (ε = 8800−10200 L mol^{-1} cm^{-1}) for all [Mn(*acen*)X] compounds, has been assigned to ligand-centered $\pi \rightarrow \pi^*$ transitions of the *acen*$^{2-}$ ligand.[65]

To make sure that the [Mn(*acen*)X] complexes are present as molecular species also in the polystyrene film samples used for the MCD measurements, the UV/vis spectra of these films were also measured. However, no additional absorption features are made out within the film spectra of any of the [Mn(*acen*)X] complexes. They are shown in the Supporting Information taking the example of [Mn(*acen*)Cl] (Supporting Information, Figures S10 and S11). It is therefore assumed that mononuclear, nonaggregated species are present in these films and that the formation of dimers, chains, or other polymeric species on the evaporation of the solvent can be ruled out. Note that the absorption bands B and C are much better resolved in the low-temperature UV/vis spectrum of the polystyrene film

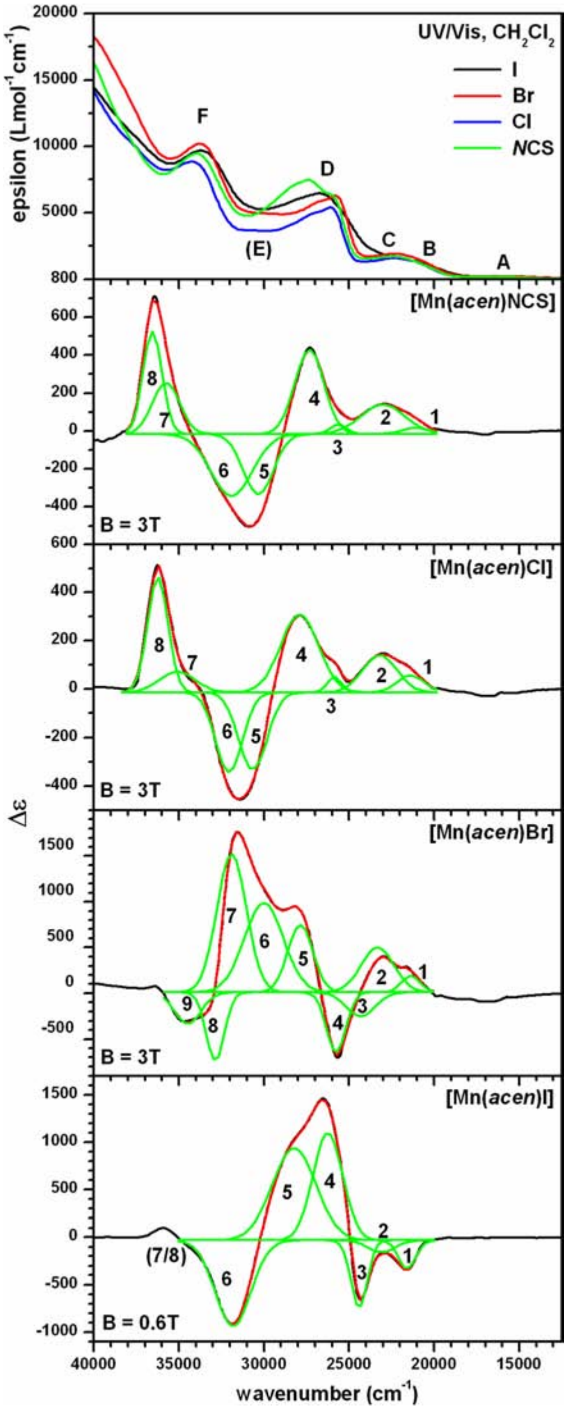

Figure 4. Low-temperature MCD spectra of the [Mn(*acen*)X] complexes measured in CH_2Cl_2/polystyrene at T = 2 K. Film samples were prepared from 1 mM complex solutions. Spectral deconvolution: Gaussian curve fits; top: UV/vis absorption spectra measured in CH_2Cl_2 at room temperature.

sample compared to the room-temperature spectrum (Supporting Information, Figure S11).

In contrast to the UV/vis absorption spectra, the low-temperature MCD spectra of the [Mn(*acen*)X] complexes are dramatically affected by the variation of the axial ligand X. Three to four broad absorption features can be identified between 20000 cm^{-1} and 38000 cm^{-1} for all [Mn(*acen*)X] complexes which were modeled with 7–9 Gaussian curves as shown in Figure 4. Taking the example of the bromido complex [Mn(*acen*)Br], it can clearly be seen from Figure 5 that the observed MCD transitions arise from a *C*-term intensity mechanism (vide supra), as they are all temperature-dependent.

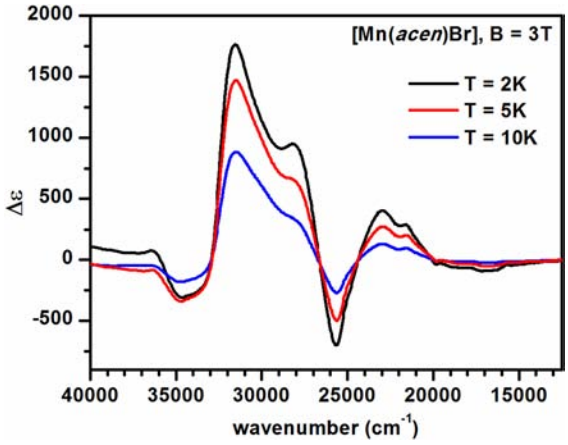

Figure 5. Low-temperature MCD spectra of [Mn(*acen*)Br] measured in CH_2Cl_2/polystyrene at *B* = 3 T and *T* = 2 K, 5 K, and 10 K. The film sample was prepared from a 1 mM complex solution.

Comparing the MCD spectra of [Mn(*acen*)Cl] and [Mn(*acen*)NCS], almost no differences are found with respect to the number, the energies and the relative intensities of the observed transitions. Specifically, four positive signed transitions are observed between 21000 cm^{-1} and 28000 cm^{-1} (bands 1–4) at positive magnetic field strengths. They are followed by two negative signed bands between 30000 cm^{-1} and 33000 cm^{-1} (bands 5, 6) and another two positive transitions around 36000 cm^{-1} (bands 7, 8). Especially in the case of the *N*CS complex, the MCD bands 4–7 show similar intensities in a positive-negative-negative-positive pattern. This indicates the presence of two oppositely signed *pseudo-A* terms which might also be considered as a "double *pseudo-A* term" feature consisting of a negative *pseudo-A* term centered at 29000 cm^{-1} (bands 4 + 5) and a positive *pseudo-A* term centered at 34000 cm^{-1} (bands 6 + 7).

In the MCD spectrum of [Mn(*acen*)Br], two positive signed bands are also found at 21400 cm^{-1} and 23300 cm^{-1} at positive magnetic field strengths (bands 1 and 2). However, in contrast to the chlorido and the *N*CS complex, an additional change of sign is observed around 25000 cm^{-1} in the MCD spectrum of the bromido complex. Compared to [Mn(*acen*)Cl] and [Mn(*acen*)NCS], the MCD bands 4 + 5 together with the bands 6 + 8 might also be considered as two oppositely signed *pseudo-A* terms adding up to a "double *pseudo-A* term" feature in the MCD spectrum of [Mn(*acen*)Br]. Compared to the former two complexes, however, it shows inverted signs (negative-positive-positive-negative) in the case of the bromido compound, that is, a positive *pseudo-A* term is centered at 26700 cm^{-1} (bands 4 + 5) and followed by a negative *pseudo-A* term around 31000–32000 cm^{-1} (bands 6 + 8). Band 7 in the MCD spectrum of [Mn(*acen*)Br] might correspond to the band 8 in the MCD spectra of [Mn(*acen*)Cl] and [Mn(*acen*)NCS] which is probably shifted to lower energies in the case of the bromido complex. It may also be assumed, that the unique negative band 3 in the MCD spectrum of the bromido complex actually is a small positive band corresponding to band 3 in the MCD spectra of [Mn(*acen*)Cl] and [Mn(*acen*)NCS] which might be hard to identify next to the large negative band 4 in the case of [Mn(*acen*)Br]. Compared to the UV/vis absorption spectra, the MCD bands 1 and 2 certainly correspond to the UV/vis transitions B and C, while the double *pseudo-A* term features match the energies of the UV/vis absorption bands D + E and F. The MCD band 3 might also be linked to the UV/vis absorption band D.

In contrast to the bromido, the chlorido, and the *N*CS complex, the MCD transitions between 20000 cm^{-1} and 25000 cm^{-1} show negative signs at positive magnetic field strengths in the case of [Mn(*acen*)I] (band 1–3). They are followed by two very intense positive transitions at 26200 cm^{-1} and 28400 cm^{-1} (bands 4, 5) and another negative transition at 31800 cm^{-1} (band 6). Bands 3–6 show the same negative-positive-positive-negative pattern of MCD intensities which was already found for the bands 4 + 5 and 6 + 8 in the MCD spectrum of the bromido complex. Corresponding to the MCD spectra of the other three complexes, these bands should therefore also be considered as two oppositely signed *pseudo-A* terms or "double *pseudo-A* terms" feature, respectively. An additional positive *pseudo-A* term can probably be made out around 35000 cm^{-1} (bands 7, 8). However, as the "double *pseudo-A* terms", independently of the individual signs, clearly shift to lower energies with the decreasing ligand field strength of the axial ligand X throughout the [Mn(*acen*)X] series, it cannot be ruled out that the small positive bands, which are identified for the other three complexes between 20000 cm^{-1} and 25000 cm^{-1}, are superimposed by the negative part of the positive *pseudo-A* term at 25000 cm^{-1} (band 3 + 4) in the case of the iodido complex. In consequence, the MCD bands 1 and 2 may actually also be positively signed in the case of [Mn(*acen*)I] corresponding to the bands 1 and 2 in the MCD spectra of [Mn(*acen*)Br], [Mn(*acen*)Cl], and [Mn(*acen*)NCS]. This may also be the explanation for the fact that the band 3 appears to have a much lower intensity than band 4 in the case of the iodido complex.

The spectral region below 20000 cm^{-1} corresponds to the UV/vis absorption band A. The MCD intensities are negative at positive magnetic field strengths for all [Mn(*acen*)X] compounds but are very low, so they will not be analyzed in detail within this paper.

The energies of the UV/vis and MCD transitions of all [Mn(*acen*)X] complexes are listed in Table 3.

Comparing the UV/vis and MCD spectra of the [Mn(*acen*)X] complexes, it becomes evident that MCD, in contrast to UV/vis absorption spectroscopy, is very sensitive to the small changes of the ligand field strength which are induced by the variation of the axial ligand X. Two oppositely signed *pseudo-A* terms or a "double *pseudo-A* term" are identified as the dominating spectral feature of the MCD spectra which, however, shows different signs for the iodido and bromido complexes compared to the chlorido and *N*CS complexes. To explain the overall sign change of the "double *pseudo-A* terms", a detailed analysis of the MCD bands is carried out in the

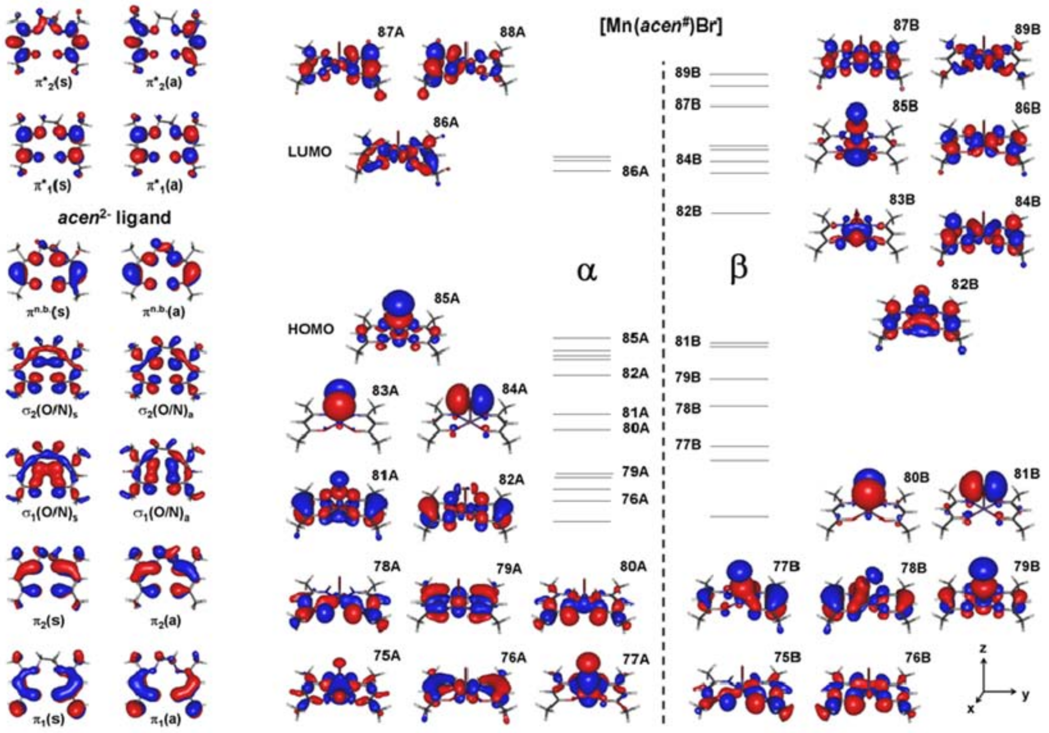

Figure 6. (left) Molecular orbitals of the *acen*$^{2-}$ ligand and (right) molecular orbitals of the symmetrized bromido complex [Mn(*acen*$^{\#}$)Br] in an idealized square-planar coordination geometry (B3LYP/def2tzvp).

following which is based on molecular orbital calculations as well as specific symmetry considerations.

DFT Computations of the Molecular Orbitals. To identify the donor and acceptor orbitals of the "double *pseudo-A* term" transitions, the molecular orbitals of the [Mn(*acen*)X] complexes were calculated using DFT. For a basic understanding of the electronic structures of these complexes, the MOs are first considered for a symmetrized system.

MOs of the *acen*$^{2-}$ Ligand. Theoretically cutting the *acen*$^{2-}$ ligand molecule between the CH_2 groups of the ethylene diamine bridge, two "halves" are obtained which contain two delocalized double bonds each. Five π-orbitals are obtained for each "half" which are two bonding π-orbitals (π_1, π_2), one nonbonding π-orbital ($\pi^{\text{n.b.}}$), and two antibonding π^*-orbitals (π_1^*, π_2^*). The molecular orbitals (MOs) of the actual *acen*$^{2-}$ ligand now can be derived from the symmetric (s) and antisymmetric (a) linear combinations of each one of these π-orbitals with the corresponding mirror images leading to a total number of 10 ligand π-orbitals (Figure 6, left). In total, 12 π-electrons have to be placed into these MOs, so that the 2 bonding and the nonbonding *acen* π-orbitals, π_1(s, a), π_2(s, a) and $\pi^{\text{n.b.}}$(s, a), are doubly occupied while the 4 π^*-orbitals, π_1^*(s, a) and π_2^*(s, a), are left unoccupied in the electronic ground state. In addition, the in-plane p-orbitals of the heteroatoms, N and O, are symmetrically (s) and antisymmetrically (a) combined to form two types of *acen* σ-orbitals, $\sigma_1(\text{O/N})_{\text{s,a}}$ and $\sigma_2(\text{O/N})_{\text{s,a}}$ (Figure 6, left).

MOs of the [Mn(*acen*)X] Complexes. The MOs of the [Mn(*acen*)X] complexes are generated by the linear combination of the *acen* ligand orbitals, the Mn d-orbitals and the p-orbitals of the apical ligand X. Their actual composition is best illustrated on the basis of the corresponding C_S symmetrical complexes exhibiting ideal square-pyramidal coordination geometries, as here no mixing of different metal and/or ligand orbitals is obtained for the individual MOs. For this purpose, the ethylene diamine bridge of the *acen*$^{2-}$ ligand was replaced by two hydrogen atoms. The resulting two planar ligand moieties (referred to as *acen*$^{\#}$) now are symmetrically arranged around the Mn(III) ion which is fixed within the equatorial plane formed by the coordinating N and O *acen* donor atoms. In the following, the results of these model calculations will be presented in detail, taking the symmetrized bromido complex [Mn(*acen*$^{\#}$)Br] as an example (Figure 6 (right), Table 2).

In general, the molecular mirror plane *xz* defines the molecular axes of a C_S symmetric molecule. The resulting MOs are then either symmetric (a′) or antisymmetric (a″) with respect to the mirror plane. Because of the very high covalence of the metal−ligand bonds, a clear distinction between metal centered d-orbitals and ligand orbitals is no longer possible. From symmetry and overlap considerations, however, only certain linear combinations can occur, and each manganese d-orbital is theoretically expected to be observed in both symmetric and antisymmetric linear combinations with the appropriate *acen* ligand orbitals and/or the p-orbitals of the axial ligand X. Strictly spoken, the dxz, dyz, and dz^2 manganese d-orbitals can only be combined with the *acen* π-orbitals, while dxy and d$x^2{-}y^2$ obviously can only interact with the σ-orbitals of the coordinating N and O *acen* ligand atoms. Because of their particular symmetries dxz, dz^2, and d$x^2{-}y^2$ might only be found in linear combinations with symmetric (s) σ- and π-orbitals of the *acen* ligand, while dyz and dxy may only be combined with antisymmetric (a) ligand orbitals. Note that the symmetric binding π-orbital π_1(s), the antisymmetric binding π-orbital π_2(a) as well as the symmetric and antisymmetric σ_1-orbitals, $\sigma_1(\text{O/N})_{\text{s}}$ and $\sigma_1(\text{O/N})_{\text{a}}$, do not interact with any of the manganese d-orbitals because of their particular symmetries.

In the symmetrized bromido complex [Mn(*acen*$^{\#}$)Br], 85 occupied *alpha* spin orbitals and 81 occupied *beta* spin orbitals

Table 2. Calculated Molecular Orbitals of the Symmetrized Complex [Mn(*acen*$^{\#}$)Br] (C_S symmetry, B3LYP/def2tzvp)

	sym[a]	composition[b]			main character	
α spin		Mn^{3+}	*acen*$^{2-}$	Br^-		
88A	a″	(xy)	π_1*(a)		*acen* π*-orbital	π_1*(a)
87[a]	a′	(xy,xz)	π_1*(s)		*acen* π*-orbital	π_1*(s)
86[a]	a″	xy	$\sigma_2(O/N)_a$		metal d-orbital (dxy), σ_2(a) antibonding, LUMO	xy/σ_2(a)
85A	a′	z^2	($\pi^{n.b.}$(s))	p_z	metal d-orbital (dz^2), p_z antibonding, HOMO	z^2/p_z
84A	a″	(yz)	($\pi^{n.b.}$(a))	p_y	bromido p-orbital	p_y
83A	a′	(xz)	(π_2(s))	p_x	bromido p-orbital	p_x
82A	a″	yz	$\pi^{n.b.}$(a)		*acen* π-orbital (dyz/p_y antibonding)	$\pi^{n.b.}$(a)$/yz$
81A	a′	z^2	$\pi^{n.b.}$(s)	p_z	*acen* π-orbital (dz^2/p_z antibonding)	$\pi^{n.b.}$(s)$/z^2$
80A	a′	x^2-y^2	$\sigma_2(O/N)_s$		metal d-orbital (dx^2-y^2)	x^2-y^2/σ_2(s)
79A	a′	xz	π_2(s)		metal d-orbital (dxz), π_2(s) antibonding	xz/π_2
78A	a″	xy	$\sigma_2(O/N)_a$		bonding analogue of MO 86A	xy/σ_2(a)
77A	a′	z^2	($\sigma_2(O/N)_s$)	p_z	bonding analogue of MO 85A	z^2/p_z
76A	a″	yz	π_1(a)		yz/π_1 metal ligand orbital	yz/π_1
75A	a′	x^2-y^2	$\sigma_2(O/N)_s$		metal d-orbital (dx^2-y^2), corresponding to MO 80A	x^2-y^2/σ_2(s)
β spin						
89B	a″	xy	$\sigma_2(O/N)_a$		metal d-orbital (dxy), p_σ antibonding	xy/σ_2(a)
87B	a′	xz	π_1*(s)		metal d-orbital (dxz), π_1*(s) antibonding	xz/π_1*(s)
86B	a″	yz	$\pi^{n.b.}$(a)		metal d-orbital (dyz), $\pi^{n.b.}$(a) antibonding	$yz/\pi^{n.b.}$(a)
85B	a′	z^2	($\pi^{n.b.}$(s))	p_z	metal d-orbital (dz^2), $\pi^{n.b.}$(s)$/p_z$ antibonding	z^2/p_z
84B	a″	yz	π_1*(a)		metal d-orbital (dyz), π_1*(a) antibonding	yz/π_1*(a)
83B	a′	x^2-y^2	$\sigma_2(O/N)_s$		metal d-orbital (dx^2-y^2), σ_2(s) antibonding	x^2-y^2/σ_2(s)
82B	a′	xz	π_1*(s)	p_x	metal d-orbital (dxz), bonding analogue of MO 87B, p_x antibonding	xz/π_1*(s)
81B	a″	(yz)	$\pi^{n.b.}$(a)	p_y	bromido p-orbital	p_y
80B	a′	(xz)	π_2(s)	p_x	bromido p-orbital	p_x
79B	a′	z^2	$\pi^{n.b.}$(s)	p_z	bromido p-orbital, z^2/p_z bonding analogue of MO 85B, $\pi^{n.b.}$(s) antibonding	z^2/p_z
78B	a″	yz	$\pi^{n.b.}$(a)	p_y	*acen* π-orbital, yz/p_y bonding analogue of MO 86B	$\pi^{n.b.}$(a)$/yz$
77B	a′	z^2	$\pi^{n.b.}$(s)	p_z	*acen* π-orbital, z^2/p_z bonding analogue of MO 85B, $\pi^{n.b.}$(s) bonding	$\pi^{n.b.}$(s)$/z^2$
76B	a′	(x^2-y^2)	$\sigma_2(O/N)_s$		bonding analogue of MO 83B	x^2-y^2/σ_2(s)
75B	a″	(xy)	$\sigma_2(O/N)_a$		bonding analogue of MO 89B	xy/σ_2(a)

[a] C_S symmetry (mirror plane xz) [b] The dominant MO contributions are determined by the corresponding orbital coefficients obtained from the DFT calculations, minor contributions are given in brackets

are obtained which perfectly corresponds to the d^4 high-spin configuration of the Mn(III) ion. The highest occupied *alpha* spin orbital is dz^2 (z^2/p_z antibonding, 85A, α-HOMO) and the lowest unoccuppied *alpha* spin orbital is dxy (86A, α-LUMO). The dx^2-y^2 is combined with the $\sigma_2(O/N)_s$ ligand orbital (x^2-y^2/σ_2(s), 80A), dxz interacts with the symmetric *acen* π_2(s) orbital (xz/π_2(s) antibonding, 79A), and dyz interacts with the antisymmetric π_1(a) ligand orbital (yz/π_1(a) antibonding, 76A). As a consequence of spin polarization, these three Mn d-orbitals are lowered in energy to a position *below* the 4p_x and 4p_y orbitals of the axial bromido ligand (83A/84A) and are not found among the four highest occupied *alpha* spin orbitals (which correspond to the four singly occupied MOs of a d^4 high-spin configuration). In fact, the bromido p-orbitals appear very high in energy and, although there are (almost) no contributions from the corresponding metal d-orbitals, unexpectedly are found among the four highest occupied *alpha* spin orbitals instead.

The *alpha* spin orbitals 77A and 78A are the bonding analogues of the α-HOMO (z^2/p_z, 85A) and α-LUMO (xy/σ_2, 86A), respectively. The *alpha* spin orbitals 81A and 82A can be considered as pure *acen* π-orbitals, $\pi^{n.b.}$(s) and $\pi^{n.b.}$(a), with only very small contributions of the corresponding Mn d-orbitals dz^2 and dyz. Also the unoccupied π*-orbitals (π_1*(s, a), 87/88A) are virtually pure *acen* ligand orbitals with very small contributions of Mn d-orbitals.

Considering the *beta* spin orbitals, the Mn d-orbitals are, of course, found among the unoccupied orbitals (82B–87B, 89B). Compared to the *alpha* spin orbitals, the same sequence is also obtained here, although there is one difference: dxz and dyz are observed twice among the unoccupied *beta* spin orbitals. The reason for that is that, in contrast to the π_1* *alpha* spin orbitals 87A and 88A (which are observed to be pure *acen* ligand orbitals, vide supra), the π_1* *beta* spin orbitals are observed to be mixed with these two Mn d-orbitals, so that dxz is found in a bonding and an antibonding linear combination with the symmetric π_1*(s) orbital (82B, 87B), while dyz is found in antibonding linear combinations with the antisymmetric π_1* orbital (84B) and the antisymmetric nonbonding π–orbital (86B).

The highest occupied *beta* spin orbitals are the three bromido p-orbitals p_z, p_x, and p_y (79B-81B) and the bonding *acen* π-/Mn d-orbitals, $\pi^{n.b.}$(s)$/z^2$ and $\pi^{n.b.}$(a)$/yz$ (77/78B). The *beta* spin orbitals 77B and 79B both are bonding analogues of the unoccupied z^2/p_z orbital (85B) which form a bonding (77B) and an antibonding linear combination with the symmetric nonbonding *acen* π-orbital $\pi^{n.b.}$(s) (79B). In analogy and especially when compared to the MOs of the unsymmetrized [Mn(*acen*)Br] complex (Supporting Information, Figure S13, vide infra), also the $\pi^{n.b.}$(a)$/yz$ and p_y orbitals (78B and 81B) can be considered as a pair of yz/p_y bonding analogues of the unoccupied yz orbital (86B).

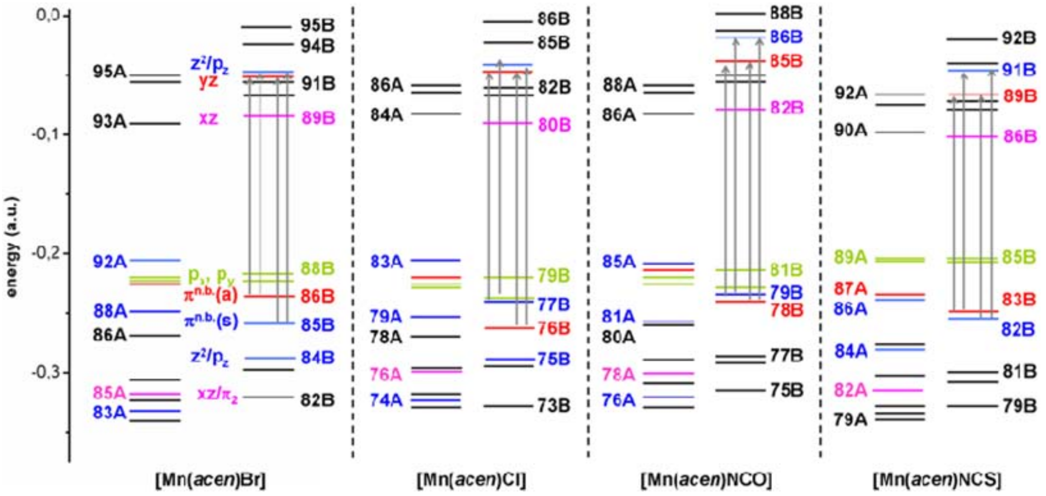

Figure 7. Relative energies of the *alpha* and *beta* spin orbitals obtained from the MO calculations of [Mn(*acen*)Br], [Mn(*acen*)Cl], [Mn(*acen*)NCO], and [Mn(*acen*)NCS] (B3LYP/def2tzvp). MCD transitions which lead to "double *pseudo-A* terms" are indicated with bold arrows.

From the DFT calculation of the molecular orbitals, and especially from the analysis of the *beta* spin orbitals, it becomes clear that, in contrast to the previous ligand field description (vide supra), d*yz* and dz^2 have to be considered as a symmetric-antisymmetric pair of Mn d-orbitals instead of d*yz* and d*xz*, as only dz^2 and d*yz* are combined with the same type of ligand orbitals which are the symmetric and antisymmetric non-bonding *acen* π-orbitals, $\pi^{\text{n.b.}}$(s) and $\pi^{\text{n.b.}}$(a).

Considering the MOs of the original, unsymmetrized complexes, the same types of orbitals are also identified for [Mn(*acen*)Br], [Mn(*acen*)Cl], and [Mn(*acen*)NCS], basically appearing in the same sequence as already described for the symmetrized bromido complex. They are given in the Supporting Information, Figures S13−S15. Because of the reduced molecular symmetries, increased mixing of different metal and/or ligand orbitals is observed. The relative energies of the *alpha* and *beta* spin orbitals are depicted in Figure 7.

Unfortunately, no reasonable results were obtained from the MO calculation of [Mn(*acen*)I] because contributions of iodide, especially to the singly occupied and unoccupied orbitals, have unrealistically high 4d (and, correspondingly, almost no 5p) orbital contributions (Supporting Information, Figure S12). This appears to reflect a deficiency of the employed basis set in the description of metal complexes with iodido ligands.

If we consider the potential overlap of metal and ligand orbitals, the only types of orbitals which are expected to be affected by the exchange of the axial ligand X are the p-orbitals of the axial ligand and the bonding and antibonding metal−ligand MOs which particularly involve dz^2, d*xz*, or d*yz*. An increase of the axial ligand field strength, associated with a shortening of the Mn−X bond length and an increasing axial displacement of the Mn(III) ion toward the axial ligand, that is, an increased pyramidalization of the Mn−N_2O_2 unit, first leads to a larger and larger reduction of the molecular symmetry and thus to an increased mixing of z^2/p_z and $\pi^{\text{n.b.}}$(s). Compared to the bromido complex, an increased splitting of the z^2/p_z and $\pi^{\text{n.b.}}(s)/z^2$ orbitals is therefore observed among the *beta* spin orbitals of the chlorido complex (75B and 77B, Figure 7, Supporting Information, Figure S14). Furthermore, the bonding $\pi^{\text{n.b.}}(a)/yz$ orbital is significantly lowered in energy when the axial ligand field strength is increased: while it is found higher in energy than $\pi^{\text{n.b.}}(s)/z^2$ in the case of [Mn(*acen*)Br], it energetically shifts *below* the $\pi^{\text{n.b.}}(s)/z^2$ orbital in the case of [Mn(*acen*)Cl].

In the case of [Mn(*acen*)NCS], the p-orbitals of the *N*CS ligand (*N*CS-$p_\pi^{\text{n.b.}}$, 88/89A and 84/85B) appear very high in energy. In contrast to [Mn(*acen*)Br] and [Mn(*acen*)Cl], they are found even higher than the dz^2 and d*yz* metal d-orbitals among the singly occupied *alpha* spin orbitals (Figure 7). As a consequence, the symmetric and antisymmetric *acen* π-orbitals $\pi^{\text{n.b.}}$(s, a) (82/83B) are *not* inverted in the calculated MO scheme in comparison to the bromido complex, as there are (almost) no contributions of *N*CS p-orbitals to these two orbitals (Supporting Information, Figure S15). Application of this MO scheme leads to wrong predictions concerning the MCD signs of the "*double pseudo-A term*" transitions (vide infra). As a possibly better model of the *N*CS complex we therefore (after proper geometry optimization) additionally determined the molecular orbitals of the [Mn(*acen*)NCO] complex (cf. Supporting Information, Figure S16). The relative MO energies of the *N*CO complex are presented between the MO energies of the chlorido and the *N*CS complex in Figure 7. In contrast to the *N*CS complex, the ligand p-orbitals of the *N*CO complex (*N*CO-$p_\pi^{\text{n.b.}}$, 82/83A and 84/85B) are not significantly lifted compared to [Mn(*acen*)Br] and [Mn(*acen*)Cl]. Among the *beta* spin orbitals, the symmetric and antisymmetric *acen* π-orbitals $\pi^{\text{n.b.}}$(s, a) of [Mn(*acen*)NCO] (78/79B) *are* inverted compared to [Mn(*acen*)Br]. In contrast to the *N*CS complex, there *are* also significant contributions of *N*CO-p_π orbitals to these two *beta* spin orbitals (Supporting Information, Figure S16).

In the following section, the "double *pseudo A*-terms" are identified to be due to MCD *C*-term transitions between two sets of *beta* spin orbitals which are $\pi^{\text{n.b.}}$(s) and $\pi^{\text{n.b.}}$(a), acting as donor orbitals, and d*yz* and dz^2, acting as acceptor orbitals. These transitions are also depicted in Figure 7. The consequences of the discussed energetic differences and shifts with respect to the signs of the MCD "double *pseudo A*-terms" are considered below.

Analysis of the MCD Spectra. The MCD spectra of the [Mn(*acen*)X] complexes roughly can be divided into three parts. The first part is the spectral region below 20000 cm^{-1} which corresponds to the broad UV/vis ligand field band A.

The MCD *C*-term intensities in this spectral region are all negative at positive magnetic field strengths, but too low to be further analyzed at this point. These broad low-intensity MCD features, however, appear to be slightly structured which indicates that more than one transition may be observed here. In addition to the spin-allowed $^5B_2 \rightarrow {}^5B_1$ quintet transition, which has been suggested by Boucher and Day[65] for the assignment of the UV/vis band A, also spin-forbidden ligand field triplet transitions might be found at these energies ($10000-15000$ cm^{-1}).

The second part of the MCD spectra is the spectral region of $20000-25000$ cm^{-1} corresponding to the UV/vis bands B and C. If we assume band 3 in the MCD spectrum of [Mn(*acen*)Br] and band 2 in the MCD spectrum of [Mn(*acen*)I] to be actually positively signed (vide supra), no big changes are observed within the series of MCD spectra in dependence of the axial ligand X at these energies. In consequence, the electronic transitions between 20000 cm^{-1} and 25000 cm^{-1} are assigned to metal-to-ligand charge transfer transitions from the singly occupied Mn d-orbitals into the π^* orbitals of the *acen* ligand, as these unoccupied MOs are not affected by the exchange of the axial ligand (Br: 94/95A, Cl: 85/86A, *N*CS: 91/92A, Figure 7) and the effect on the Mn d-orbitals is expected to be quite small. An *A*-*K* coupling mechanism might be assumed for the origin of these MCD *C*-term intensities which would explain the comparatively low intensities of these transitions.

In the third part of the MCD spectra, which is the spectral region above 25000 cm^{-1}, the most intense of all MCD transitions are observed as well as the most remarkable differences within [Mn(*acen*)X] series. It is dominated by four transitions of similar intensities which show a symmetric pattern of positive-negative-negative-positive and negative-positive-positive-negative MCD signs, respectively. These characteristic features are suggested to be due to the presence of two related, oppositely signed, *pseudo-A* terms which are also referred to as "double *pseudo-A* terms" and have previously been identified to be the dominating features in the MCD spectra of C_S symmetric transition metal complexes.[60,84] In general, the presence of a "double *pseudo-A* term" implies that both the donor and acceptor orbitals of the considered transitions derive from two pairs of (almost) degenerate orbitals of appropriate symmetry.[39,60]

In the calculated MO schemes of the [Mn(*acen*)X] complexes, several pairs of almost or formerly degenerate orbitals can be identified: (i) the symmetric and antisymmetric *acen* π^*-orbitals, π_1(s, a), (ii) the p_x and p_y orbitals of the axial ligands X, (iii) the symmetric and antisymmetric bonding *acen* π/Mn-d-orbitals $\pi^{\text{n.b.}}(\text{s})/z^2$ and $\pi^{\text{n.b.}}(\text{a})/yz$, in the following also simply referred to as *acen* π-orbitals, $\pi^{\text{n.b.}}$(s, a), and (iv) the dz^2 and d*yz* Mn d-orbitals (vide supra). However, only ligand-to-metal charge transfer (LMCT) from the *acen* π-orbitals, $\pi^{\text{n.b.}}$(s) and $\pi^{\text{n.b.}}$(a), into the singly occupied Mn d-orbitals d*yz* and dz^2 can give rise to two oppositely signed *pseudo-A* terms. This therefore is the only possible assignment for the observed "double *pseudo-A* terms" in the MCD spectra of the [Mn(*acen*)X] complexes. Because of the particular symmetries of these four orbitals, the considered transitions are the only MCD transitions that meet the three basic requirements for nonzero *C*-term intensities which are (i) the acceptor orbitals (d*yz* and dz^2) interact through spin−orbit coupling (via l_x, *J*-*K* coupling), (ii) the individual transitions have electric dipole intensity, and (iii) they are polarized in different directions perpendicular to the orbital momentum vector, that is, in the *y*- and *z*-direction in this case (and also perpendicular to the molecular mirror plane *xz*, cf. Figure 8 and Supporting Information, Figures S17−S19).

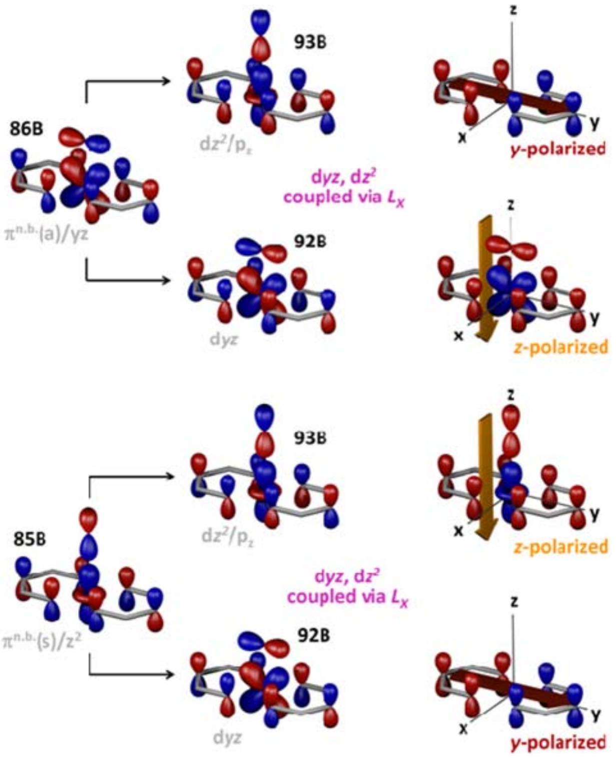

Figure 8. Transition dipole moments of the $\pi^{\text{n.b.}}$(s, a) → *yz*, z^2 transitions of [Mn(*acen*)Br] determined from the considered transition densities based on the calculated MOs (B3LYP/def2tzvp).

This directly leads us to the theoretical description of the MCD *C*-term intensities of the $\pi^{\text{n.b.}}$(s, a) → *yz*, z^2 LMCT transitions. Assuming a *J*-*K* coupling mechanism (vide supra), it is given by

$$\frac{\Delta\varepsilon}{E} \sim -\sum_{K\neq A,J} \frac{\overline{L}_x^{KJ}}{\Delta_{KJ}} (\vec{D}_y^{AK} \vec{D}_z^{AJ} - \vec{D}_z^{AK} \vec{D}_y^{AJ})$$

$$= -\sum_{K\neq A,J} \frac{\langle K|\overline{L}_x|J\rangle}{\Delta_{KJ}} \{\langle A|\mu_y|K\rangle\langle A|\mu_z|J\rangle$$

$$- \langle A|\mu_z|K\rangle\langle A|\mu_y|J\rangle\}$$

as only the effective transitions dipole moment $M_{yz}{}^{\text{eff}}$ generally has to be considered in the case of *yz*-polarized transitions. The considered electronic transitions are type I transitions, that is, electronic transitions from doubly occupied ligand orbitals into singly occupied Mn d-orbitals; the excited states thus are given by single-determinant expressions.[85] In consequence, there is a straightforward correlation between states and orbitals, and the effective transitions dipole moments can directly be expressed in terms of orbitals. The transition dipole matrix elements are then written as

$$(d_y^{ak} d_z^{aj} - d_z^{ak} d_y^{aj}) = (\langle\psi_a|\mu_y|\psi_k\rangle\langle\psi_a|\mu_z|\psi_j\rangle$$

$$- \langle\psi_a|\mu_z|\psi_k\rangle\langle\psi_a|\mu_y|\psi_z\rangle)$$

where *a* is the donor orbital and *j* and *k* are the acceptor orbitals (*j*-*k* coupling) of individual transitions *A* → *J* and *A* →

K, respectively. The corresponding orbital momentum matrix element is given by

$$\langle \psi_k | l_x | \psi_j \rangle$$

Attention must be paid to the fact that the $\pi^{\text{n.b.}}(\text{s, a}) \rightarrow yz, z^2$ transitions actually are transitions between *beta* spin orbitals. In consequence, an additional negative coefficient must be introduced to the general expression of the MCD *C*-term intensity, as the reduced spin−orbit coupling matrix element of two *beta* spin orbitals is given by

$$\langle \overline{\psi}_k | l_x s_0 | \overline{\psi}_j \rangle = -\frac{1}{2} \langle \psi_k | l_x | \psi_j \rangle$$

The MCD signs of the individual $\pi^{\text{n.b.}}(\text{s, a}) \rightarrow yz, z^2$ transitions are now determined from the corresponding transition densities based on the calculated MOs, beginning with [Mn(*acen*)Br]. At this point, it should be noted that only the symmetry of the donor orbitals determines the signs of *pseudo-A* term transitions.[39,60]

In the case of the bromido complex [Mn(*acen*)Br], the $\pi^{\text{n.b.}}(\text{a})/yz \rightarrow yz$ transition (86B → 92B) is *z*-polarized in the negative direction, while the $\pi^{\text{n.b.}}(\text{a})/yz \rightarrow z^2$ transition (86B → 93B) is *y*-polarized in the positive direction (Figure 8). Considering the $\pi^{\text{n.b.}}(\text{a})/yz \rightarrow yz$ transition, it is noted that the only contribution to the corresponding transition density does *not* involve the *acen* π-orbitals but merely arises from a yz/p_y bonding → antibonding transition along the *z* axis.

The MCD *C*-term intensity of the $\pi^{\text{n.b.}}(\text{a})/yz \rightarrow yz$ transition ($a \rightarrow j$ (86B → 92B); k: z^2 (93B)) then results to have a negative sign. Based on the above equations, it is given by

$$\begin{aligned} \frac{\Delta\varepsilon}{E} &\sim \frac{\text{Im}(\langle z^2 | l_x | yz \rangle)}{\Delta_{KJ}} \{ \langle \pi^{n.b.}(a) | \mu_y | z^2 \rangle \langle \pi^{n.b.}(a) | \mu_z | yz \rangle \\ &\quad - \langle \pi^{n.b.}(a) | \mu_z | z^2 \rangle \langle \pi^{n.b.}(a) | \mu_y | yz \rangle \} \\ &= \frac{(+1)}{\Delta_{KJ}} \{ (+1) | \langle \pi^{n.b.}(a) | \mu_y | z^2 \rangle | \cdot (-1) | \langle \pi^{n.b.}(a) | \mu_z | yz \rangle | - 0 \} \\ &< 0 \end{aligned}$$

with $\Delta_{KJ} = E_K - E_J > 0$, while the MCD *C*-term intensity of the corresponding $\pi^{\text{n.b.}}(\text{a})/yz \rightarrow z^2$ transition ($a \rightarrow j$ (86B → 93B); k: yz (92B)) has a positive sign

$$\begin{aligned} \frac{\Delta\varepsilon}{E} &\sim \frac{\text{Im}(\langle yz | l_x | z^2 \rangle)}{\Delta_{KJ}} \{ \langle \pi^{n.b.}(a) | \mu_y | yz \rangle \langle \pi^{n.b.}(a) | \mu_z | z^2 \rangle \\ &\quad - \langle \pi^{n.b.}(a) | \mu_z | yz \rangle \langle \pi^{n.b.}(a) | \mu_y | z^2 \rangle \} \\ &= \frac{(-1)}{\Delta_{KJ}} \{ 0 - (-1) | \langle \pi^{n.b.}(a) | \mu_z | yz \rangle | \cdot (+1) | \langle \pi^{n.b.}(a) | \mu_y | z^2 \rangle | \} \\ &> 0 \end{aligned}$$

with $\Delta_{KJ} = E_K - E_J < 0$.

Taken together, the $\pi^{\text{n.b.}}(\text{a})/yz \rightarrow yz, z^2$ transitions (86B → 92/93B) give rise to a positive *pseudo-A* term and are therefore assigned to the MCD bands 4 and 5 in the MCD spectrum of [Mn(*acen*)Br] which also correspond to the bands 3 and 4 in the MCD spectrum of the iodido complex.

The same procedure is applied to analyze the $\pi^{\text{n.b.}}(\text{s})/z^2 \rightarrow yz, z^2$ transitions (85B → 92/93B). As inferred from Figure 8, the $z^2/\pi^{\text{n.b.}}(\text{s}) \rightarrow yz$ transition is *y*-polarized in the positive direction and the $\pi^{\text{n.b.}}(\text{s})/z^2 \rightarrow z^2$ transition is *z*-polarized in the negative direction. Again, the only contribution to the transition density of the latter transition, corresponding to the $\pi^{\text{n.b.}}(\text{a})/yz \rightarrow yz$ transition (vide supra), does not involve the *acen* π-orbitals but only arises from a z^2/p_z bonding → antibonding transition along the *z* axis. From that it becomes clear that the $\pi^{\text{n.b.}}(\text{s, a}) \rightarrow yz, z^2$ LMCT transitions arise from the interplay of in-plane and out-of-plane electronic transitions (perpendicular to the molecular mirror plane *xz*).

A positive MCD *C*-term intensity is obtained for the $\pi^{\text{n.b.}}(\text{s})/z^2 \rightarrow yz$ transition ($a \rightarrow j$ (85B → 92B); k: z^2 (93B)):

$$\begin{aligned} \frac{\Delta\varepsilon}{E} &\sim \frac{\text{Im}(\langle z^2 | l_x | yz \rangle)}{\Delta_{KJ}} \{ \langle \pi^{n.b.}(s) | \mu_y | z^2 \rangle \langle \pi^{n.b.}(s) | \mu_z | yz \rangle \\ &\quad - \langle \pi^{n.b.}(s) | \mu_z | z^2 \rangle \langle \pi^{n.b.}(s) | \mu_y | yz \rangle \} \\ &= \frac{(+1)}{\Delta_{KJ}} \{ 0 - (-1) | \langle \pi^{n.b.}(s) | \mu_z | z^2 \rangle | \cdot (+1) | \langle \pi^{n.b.}(s) | \mu_y | yz \rangle | \} \\ &> 0 \end{aligned}$$

with $\Delta_{KJ} = E_K - E_J > 0$, while the corresponding $\pi^{\text{n.b.}}(\text{s})/z^2 \rightarrow z^2$ transition (85B → 73B ($a \rightarrow j$); k: yz (92B)) results in a negative signed MCD band

$$\begin{aligned} \frac{\Delta\varepsilon}{E} &\sim \frac{\text{Im}(\langle yz | l_x | z^2 \rangle)}{\Delta_{KJ}} \{ \langle \pi^{n.b.}(s) | \mu_y | yz \rangle \langle \pi^{n.b.}(s) | \mu_z | z^2 \rangle \\ &\quad - \langle \pi^{n.b.}(s) | \mu_z | yz \rangle \langle \pi^{n.b.}(s) | \mu_y | z^2 \rangle \} \\ &= \frac{(-1)}{\Delta_{KJ}} \{ (+1) | \langle \pi^{n.b.}(s) | \mu_y | yz \rangle | \cdot (-1) | \langle \pi^{n.b.}(s) | \mu_z | z^2 \rangle | - 0 \} \\ &< 0 \end{aligned}$$

with $\Delta_{KJ} = E_K - E_J < 0$.

Taken together, the $\pi^{\text{n.b.}}(\text{s})/z^2 \rightarrow yz, z^2$ LMCT transitions (85B → 92/93B) thus lead to a negative *pseudo-A* term. They are assigned to the bands 6 and 8 in the MCD spectrum of [Mn(*acen*)Br] which correspond to the bands 5 and 6 in the MCD spectrum of [Mn(*acen*)I]. To sum up, the $\pi^{\text{n.b.}}(\text{s, a}) \rightarrow yz, z^2$ transitions give rise to two related, oppositely signed *pseudo-A* terms, that is, a "double *pseudo-A* term" in the MCD spectrum of [Mn(*acen*)Br] which is illustrated in Figure 9.

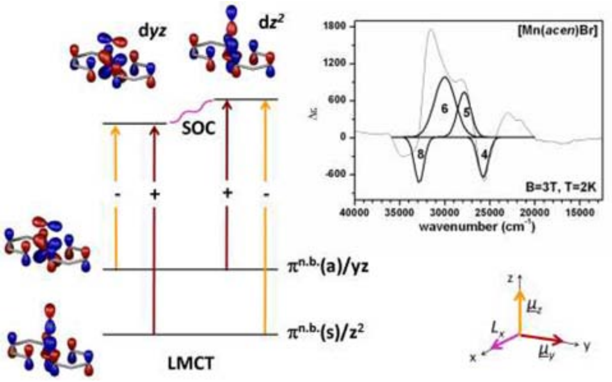

Figure 9. Assignment of the "double *pseudo-A* term" feature in the low-temperature MCD spectrum of [Mn(*acen*)Br] to the $\pi^{\text{n.b.}}(\text{s, a}) \rightarrow yz, z^2$ LMCT transitions based on MO considerations. The same signs of the "double *pseudo*-A term" transitions are also observed on the MCD spectrum of [Mn(*acen*)I].

In the case of the chlorido complex, the transition dipole moments of the $\pi^{\text{n.b.}}(\text{a})/yz \rightarrow yz, z^2$ transitions (76B → 83/84B) show the same signs as for the bromido complex, while the transition dipole moments of the $\pi^{\text{n.b.}}(\text{s})/z^2 \rightarrow yz, z^2$ transitions (77B → 83/84B) both flip compared to [Mn(*acen*)Br] (Supporting Information, Figure S17). However, based on the used equations of the MCD *C*-term intensity (vide supra), this would not invert the signs of the "double *pseudo-A* term“ transitions in the MCD spectrum of [Mn(*acen*)Cl]. In contrast, the only reason for that change of signs is that the symmetric and the antisymmetric *acen* π-orbitals $\pi^{\text{n.b.}}$(s, a) are inverted in energy in the MO scheme of [Mn(*acen*)Cl] compared to the bromido complex. As already mentioned, this is due to a higher stabilization of the bonding $\pi^{\text{n.b.}}$(a)/*yz* orbital in consequence of the higher axial displacement of the Mn(III) ion associated with a larger reduction of symmetry on the increased ligand field strength of the axial ligand X (vide supra). As this inversion is associated with the change of the symmetry within the donor orbitals, the positive and negative *pseudo-A* terms are inverted in the MCD spectrum of [Mn(*acen*)Cl] which leads to the observed change of signs within the “double *pseudo-A* term” feature (Figure 10).

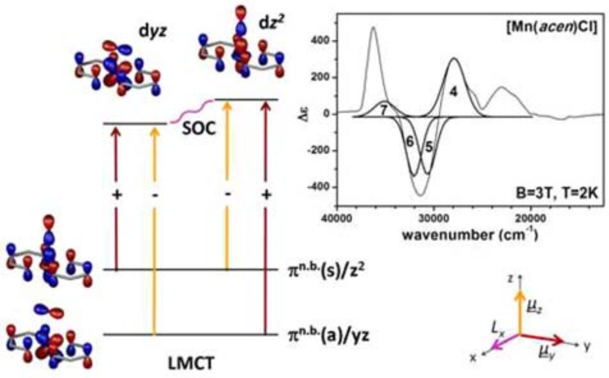

Figure 10. Assignment of the “double *pseudo-A* term” feature in the low-temperature MCD spectrum of [Mn(*acen*)Cl] to the $\pi^{\text{n.b.}}$(s, a) → *yz*, z^2 LMCT transitions based on MO considerations. The same signs of the “double *pseudo*-A term” transitions are also observed on the MCD spectrum of [Mn(*acen*)NCS].

The MCD spectrum of the *NCS* complex is very similar to that of the chlorido complex; that is, a change of signs within the “double *pseudo-A* term” is also observed compared to the iodido and bromido complexes. This obviously confirms the described trends: the MOs, which are involved in the considered MCD transitions, energetically shift in dependence of the axial ligand field strength; this leads to the inversion of the symmetry within the donor orbitals in the case of the chlorido and *NCS* complexes and thus a change of signs is observed within the “double *pseudo-A* terms” compared to the iodido and bromido complexes. In the calculated MO scheme, however, the symmetric and antisymmetric *acen* π-orbitals $\pi^{\text{n.b.}}$(s, a) of the *NCS* complex are *not* inverted compared to [Mn(*acen*)Br] (Figure 7 and Supporting Information, Figure S15). On the other hand, phase changes occur in the calculated $\pi^{\text{n.b.}}$(a)/*yz* and *yz* orbitals of the *NCS* complex (83B, 89B, Supporting Information, Figure S15) compared to the bromido complex. This leads to a change of signs in the above equations of the MCD *C*-term intensity compared to [Mn(*acen*)Br], as the signs of the transition dipole moments of the $\pi^{\text{n.b.}}$(s) → *yz* and the $\pi^{\text{n.b.}}$(a) → z^2 transitions are inverted (both being polarized in the *negative y*-direction in the case of [Mn(*acen*)-NCS], Supporting Information, Figure S18). In addition, the signs of the spin−orbit coupling matrix elements change. In summary, this causes a double change of sign (the transition dipole moments of the remaining $\pi^{\text{n.b.}}$(s) → z^2 and $\pi^{\text{n.b.}}$(a) → *yz* transitions do *not* change their signs compared to [Mn(*acen*)Br]; Supporting Information, Figure S18). So the $\pi^{\text{n.b.}}$(s, a)→ *yz*, z^2 “double *pseudo-A* term” transitions of the *NCS* complex do *not* change their overall signs compared to the bromido complex. Accordingly, there is *no* formal explanation for the inverted signs of the “double *pseudo-A* term” in the MCD spectrum of [Mn(*acen*)NCS] compared to the spectra of [Mn(*acen*)I] and [Mn(*acen*)Br] based on the calculated MOs of the *NCS* complex.

However, as we have already assumed, the atomic orbital contributions and the relative energies of calculated MOs might be incorrect in the case of the [Mn(*acen*)NCS] complex because the NCS-$p_\pi^{\text{n.b.}}$ orbitals appear too high in energy and do not contribute to the nonbonding *acen* π-orbitals $\pi^{\text{n.b.}}$(s, a). Looking at the MOs of the corresponding *NCO* complex, we note that no phase changes (compared to [Mn(*acen*)Br]) are observed in any of the involved orbitals (Supporting Information, Figure S16). The individual transition dipole moments therefore retain their signs compared to the bromido complex, but the symmetric and antisymmetric *acen* π-orbitals $\pi^{\text{n.b.}}$(s, a) of the [Mn(*acen*)NCO] complex, in contrast to the *NCS* complex, *are* inverted compared to [Mn(*acen*)Br]. This leads to an overall sign change of the corresponding “double *pseudo-A* term” transitions (Supporting information, Figure S19) with respect to the bromido complex and a MCD spectrum similar to that of the chlorido complex, as observed

Table 3. Assignment of the MCD and UV/vis Transitions of the [Mn(*acen*)X] Complexes Based on Molecular Orbital and Symmetry Considerations

UV/vis	[Mn(*acen*)I]	[Mn(*acen*)Br]	[Mn(*acen*)Cl]	[Mn(*acen*)NCS]	assignment
(A) 16400	16400 (−)	16400 (−)	16400 (−)	16400 (−)	d-d ligand field transitions
(B, C) 22300	(1) 21600 (−)	(1) 21400 (+)	(1) 21400 (+)	(1) 21400 (+)	metal-to-ligand charge transfer into *acen* π*-orbitals
	(2) 23300 (−)	(2) 23300 (+)	(2) 23200 (+)	(2) 23200 (+)	
	(3) 24400 (−)	(3) 24300 (−)			
(D) 25000−27000	(4) 26200 (+)	(4) 25800 (−)	(3) 25900 (+)	(3) 25300 (+)	ligand-to-metal charge transfer-“double pseudo-A terms”: $\pi^{\text{n.b.}}$(s, a)→ *yz*, z^2
	(5) 28400 (+)	(5) 27900 (+)	(4) 27900 (+)	(4) 27500 (+)	
(E) 30500[a]		(6)30000 (+)	(5) 30700 (−)	(5) 30700 (−)	
	(6) 31800 (−)	(7) 31900 (+)	(6) 32100 (−)	(6) 32800 (−)	
(F) 33500		(8) 32900 (−)			
	(7)	(9) 34500 (−)			
	(8)		(7) 35100 (+)	(7) 35800 (+)	
			(8) 36300 (+)	(8) 36400 (+)	

[a] [Mn(*acen*)Br] and [Mn(*acen*)Cl].

experimentally. The *N*CO complex thus in fact is found to provide a better theoretical description of the *N*CS complex.

Finally, it might be noted that the splitting of the donor and acceptor orbitals appears to be different in the calculated MO schemes of the bromido and chlorido complexes compared to the *N*CS and *N*CO complexes (Figure 7). While the splitting of the $\pi^{\text{n.b.}}$(s, a) donor orbitals is large and d*yz* and dz^2 are almost degenerate in the case of [Mn(*acen*)Br] and [Mn(*acen*)Cl], the donor orbitals are almost degenerate and the splitting between d*yz* and dz^2 is large for [Mn(*acen*)NCS] and [Mn(*acen*)NCO]. However, given that these splittings have been calculated correctly by DFT, this ultimately does not affect the signs of the "double *pseudo-A* terms" in the MCD spectra of the [Mn(*acen*)X] complexes.

The assignments of the low-temperature MCD spectra of the [Mn(*acen*)X] complexes are collected in Table 3.

SUMMARY AND CONCLUSION

Detailed spectroscopic and theoretical investigations have been performed on a series of [Mn(*acen*)X] Schiff base complexes (X^- = I^-, Br^-, Cl^-, *N*CS^-). The individual compounds first have been thoroughly characterized by vibrational spectroscopy. The molecular vibrations were completely assigned and correlated to the observed transitions based on quantum chemical computations of the IR and Raman spectra. As a result, the DFT optimized complex structures were verified as reliable for the subsequent MO calculations.

The analysis of the [Mn(*acen*)X] low-temperature parallel mode cw X-band EPR spectra provided excellent results with respect to the quality of the recorded spectra as well as of the spectral simulations. From this study it could be concluded, that nonaggregated, mononuclear Mn(III) species are present in solution. This was the most important prerequisite for the subsequent UV/vis and MCD studies. Additionally, it was found that the variation of the axial ligand X has no effect on the EPR spectra.

The UV/vis absorption spectra of the [Mn(*acen*)X] complexes have already been reported in the literature[65] but were further examined within this work with respect to different solvents and different matrixes (polystyrene film spectra vs solution spectra). Also low-temperature UV/vis spectra have been recorded. It could be confirmed that varying ligand field strengths due to different axial ligands X ($I^- < Br^- < Cl^- <$ *N*CS^-) have almost no effect on the UV/vis absorption spectra.

The low-temperature MCD spectra of the [Mn(*acen*)X] complexes, in contrast, were found to be dramatically affected by the variation of the axial ligand X, impressively demonstrating the extreme sensitivity of this technique to small changes of the ligand field. Specifically, two very intense, oppositely signed *pseudo-A* terms, referred to as "double *pseudo-A* terms", were identified as the dominant spectral features. Comparing the MCD spectra of [Mn(*acen*)I] and [Mn(*acen*)-Br] to the those of [Mn(*acen*)Cl] and [Mn(*acen*)NCS], an overall sign change occurred within these features which was analyzed based on MO calculations and symmetry considerations. For that purpose, the MOs were calculated by spin-unrestricted DFT computations. A theoretical description of the calculated MOs was achieved with the help of the C_S-symmetrized [Mn(*acen*$^{\#}$)Br] complex. From that analysis, it was deduced that the observed "double *pseudo-A* terms" derive from $\pi^{\text{n.b.}}$(s, a) $\rightarrow yz$, z^2 ligand-to-metal charge transfer transitions. The MCD sign change observed throughout the [Mn(*acen*)X] series was explained by the inversion of the energetic sequence of the symmetric and antisymmetric *acen* π-orbitals $\pi^{\text{n.b.}}$(s) and $\pi^{\text{n.b.}}$(a) due to changes in the electronic structure of the complexes induced by the axial ligand X.

The observed sensitivity of the MCD spectra on the axial ligands—in contrast to optical absorption and EPR spectroscopy—potentially renders this method useful to elucidate the coordination of active sites in biology. In these applications the axial ligand may be an exogenous ligand like water, a ligand added as a spectroscopic probe like azide, or the substrate, and MCD can be used as a "fingerprint" method to probe the coordination of these molecules to the active site. In addition, MCD strongly depends on the geometry of the active site, as the MCD spectra of square-pyramidal Mn complexes (like those presented in this study) drastically differ from those obtained from, for example, trigonal-bipyramidal Mn sites as present in MnSOD.[55,56] These differences can also be used to gain information on the geometric structure of biological metal centers.

In summary, considerable insight into the electronic structure and the spectroscopic properties of the series of complexes [Mn(*acen*)X], X = *N*CS, Cl, Br, and I, has been achieved. The spectroscopic data have been analyzed with the help of DFT calculations, allowing to understand both the trends in the MCD spectra and the qualitative differences between the UV/vis and MCD data. These results also clearly demonstrate that the correlation between both methods is by no means trivial. Although both methods are based on electric-dipole mechanisms, MCD spectra depend on more special selection rules (as shown here for the *C*-term mechanism) which may lead to dominant spectral features for electronic transitions that only little influence the appearance of the corresponding optical absorption spectra.

ASSOCIATED CONTENT

Ⓢ Supporting Information

Includes the results of the elemental analyses (Table S1), the analysis of the vibrational spectra of [Mn(*acen*)Br] (Figure S1, Table S2), additional low-temperature parallel mode EPR spectra, the analysis of temperature-dependent EPR measurements and spectral simulations (Figures S2−S8). Also the absorption spectra of [Mn(*acen*)Br] in different coordinating and noncoordinating solvents are presented (Figures S9) as well as the comparison of the solution and the (low-temperature) polystyrene film UV/vis absorption spectra using the example of [Mn(*acen*)Cl] (Figures S10 and S11). Furthermore, the calculated MOs of the unsymmetrized [Mn(*acen*)X] complexes are included (Figures S12−S16) as well as the transition dipole moments of the $\pi^{\text{n.b.}}$(s, a) $\rightarrow$ *yz*, z^2 transitions of [Mn(*acen*)Cl], [Mn(*acen*)NCS], and [Mn(*acen*)-NCO] (Figures S17−S19). The Cartesian coordinates of the geometry optimized complex structures for all [Mn(*acen*)X] compounds are given in the Tables S4−S9. This material is available free of charge via the Internet at http://pubs.acs.org.

AUTHOR INFORMATION

Corresponding Author

*E-mail: ftuczek@ac.uni-kiel.de. Phone: +49 431 880-1410. Fax: +49 431 880-1520.

Notes

The authors declare no competing financial interest.

■ ACKNOWLEDGMENTS

The authors kindly thank Wulf Thimm for theoretical support concerning the MO calculations. They also thank Holger Naggert for measuring the low-temperature UV/vis absorption spectrum of [Mn(*acen*)Cl] which is given in the Supporting Information. Ph.K. acknowledges a Liebig fellowship by Fonds der Chemischen Industrie.

■ REFERENCES

(1) Fridovich, I. *Annu. Rev. Biochem.* **1995**, *64*, 97−112.
(2) Edwards, R. A.; Baker, H. M.; Whittaker, M. M.; Whittaker, J. W.; Jameson, G. B.; Baker, E. N. *J. Biol. Inorg. Chem.* **1998**, *3*, 161−171.
(3) Sheng, Y.; Stich, T. A.; Barnese, K.; Gralla, E. B.; Cascio, D.; Britt, R. D.; Cabelli, D. E.; Valentine, J. S. *J. Am. Chem. Soc.* **2011**, *133*, 20878−20889.
(4) Antonyuk, S. V.; Melik-Adamyan, V. R.; Popov, A. N.; Lamzin, V. S.; Hempstead, P. D.; Harrison, P. M.; Artymyuk, P. J.; Barynin, V. V. *Crystallogr. Rep.* **2000**, *45*, 105−116.
(5) Barynin, V. V.; Whittaker, M. M.; Antonyuk, S. V.; Lamzin, V. S.; Harrison, P. M.; Artymiuk, P. J.; Whittaker, J. W. *Structure* **2001**, *9*, 725−738.
(6) Umena, Y.; Kawakami, K.; Shen, J. R.; Kamiya, N. *Nature* **2011**, *473*, 55−60.
(7) Loll, B.; Kern, J.; Saenger, W.; Zouni, A.; Biesiadka, J. *Nature* **2005**, *438*, 1040−1044.
(8) Ferreira, K. N.; Iverson, T. M.; Maghlaoui, K.; Barber, J.; Iwata, S. *Science* **2004**, *303*, 1831−1838.
(9) Kok, B.; Forbush, B.; Mcgloin, M. *Photochem. Photobiol.* **1970**, *11*, 457−475.
(10) Dau, H.; Limberg, C.; Reier, T.; Risch, M.; Roggan, S.; Strasser, P. *ChemCatChem.* **2010**, *2*, 724−761.
(11) Meyer, T. J.; Huynh, M. H.; Thorp, H. H. *Angew. Chem., Int. Ed.* **2007**, *46*, 5284−5304.
(12) Lubitz, W.; Reijerse, E. J.; Messinger, J. *Energy Environ. Sci.* **2008**, *1*, 15−31.
(13) Sproviero, E. M.; Gascon, J. A.; McEvoy, J. P.; Brudvig, G. W.; Batista, V. S. *Coord. Chem. Rev.* **2008**, *252*, 395−415.
(14) Batinić-Haberle, I.; Reboucas, J. S.; Spasojevic, I. *Antioxid. Redox Signaling* **2010**, *13*, 877−918.
(15) Wu, A. J.; Penner-Hahn, J. E.; Pecoraro, V. L. *Chem. Rev.* **2004**, *104*, 903−938.
(16) de Boer, J. W.; Browne, W. R.; Feringa, B. L.; Hage, R. *C. R. Chim.* **2007**, *10*, 341−354.
(17) Mukhopadhyay, S.; Mandal, S. K.; Bhaduri, S.; Armstrong, W. H. *Chem. Rev.* **2004**, *104*, 3981−4026.
(18) Berggren, G.; Thapper, A.; Huang, P.; Eriksson, L.; Styring, S.; Anderlund, M. F. *Inorg. Chem.* **2011**, *50*, 3425−3430.
(19) Triller, M. U.; Hsieh, W. Y.; Pecoraro, V. L.; Rompel, A.; Krebs, B. *Inorg. Chem.* **2002**, *41*, 5544−5554.
(20) Berends, H. M.; Manke, A. M.; Näther, C.; Tuczek, F.; Kurz, P. *Dalton Trans.* **2012**, *41*, 6215−6224.
(21) Evelo, R. G.; Styring, S.; Rutherford, A. W.; Hoff, A. J. *Biochim. Biophys. Acta* **1989**, *973*, 428−442.
(22) Zheng, M.; Khangulov, S. V.; Dismukes, G. C.; Barynin, V. V. *Inorg. Chem.* **1994**, *33*, 382−387.
(23) Pessiki, P. J.; Khangulov, S. V.; Ho, D. M.; Dismukes, G. C. *J. Am. Chem. Soc.* **1994**, *116*, 891−897.
(24) Khangulov, S. V.; Pessiki, P. J.; Barynin, V. V.; Ash, D. E.; Dismukes, G. C. *Biochemistry* **1995**, *34*, 2015−2025.
(25) Dismukes, G. C. *Chem. Rev.* **1996**, *96*, 2909−2926.
(26) Meier, A. E.; Whittaker, M. M.; Whittaker, J. W. *Biochemistry* **1996**, *35*, 348−360.
(27) Peterson, S.; Ahrling, K. A.; Styring, S. *Biochemistry* **1999**, *38*, 15223−15230.
(28) Campbell, K. A.; Yikilmaz, E.; Grant, C. V.; Gregor, W.; Miller, A. F.; Britt, R. D. *J. Am. Chem. Soc.* **1999**, *121*, 4714−4715.
(29) Peloquin, J. M.; Campbell, K. A.; Randall, D. W.; Evanchik, M. A.; Pecoraro, V. L.; Armstrong, W. H.; Britt, R. D. *J. Am. Chem. Soc.* **2000**, *122*, 10926−10942.
(30) Campbell, K. A.; Force, D. A.; Nixon, P. J.; Dole, F.; Diner, B. A.; Britt, R. D. *J. Am. Chem. Soc.* **2000**, *122*, 3754−3761.
(31) Campbell, K. A.; Lashley, M. R.; Wyatt, J. K.; Nantz, M. H.; Britt, R. D. *J. Am. Chem. Soc.* **2001**, *123*, 5710−5719.
(32) Peloquin, J. M.; Britt, R. D. *Biochim. Biophys. Acta* **2001**, *1503*, 96−111.
(33) Bernat, G.; Morvaridi, F.; Feyziyev, Y.; Styring, S. *Biochemistry* **2002**, *41*, 5830−5843.
(34) Schäfer, K. O.; Bittl, R.; Lendzian, F.; Barynin, V.; Weyhermüller, T.; Wieghardt, K.; Lubitz, W. *J. Phys. Chem. B* **2003**, *107*, 1242−1250.
(35) Huang, P.; Kurz, P.; Styring, S. *Appl. Magn. Reson.* **2007**, *31*, 301−320.
(36) Scheifele, Q.; Riplinger, C.; Neese, F.; Weihe, H.; Barra, A. L.; Juranyi, F.; Podlesnyak, A.; Tregenna-Piggott, P. L. W. *Inorg. Chem.* **2008**, *47*, 439−447.
(37) Berggren, G.; Thapper, A.; Huang, P.; Kurz, P.; Eriksson, L.; Styring, S.; Anderlund, M. F. *Dalton Trans.* **2009**, 10044−10054.
(38) Sheng, Y. W.; Stich, T. A.; Barnese, K.; Gralla, E. B.; Cascio, D.; Britt, R. D.; Cabelli, D. E.; Valentine, J. S. *J. Am. Chem. Soc.* **2011**, *133*, 20878−20889.
(39) Neese, F.; Solomon, E. I. *Inorg. Chem.* **1999**, *38*, 1847−1865.
(40) Solomon, E. I.; Lever, A. B. P. *Inorganic Electronic Structure and Spectroscopy*; Whiley Interscience: Hoboken, NJ, 2006; Vol. *I*.
(41) Solomon, E. I.; Pavel, E. G.; Loeb, K. E.; Campochiaro, C. *Coord. Chem. Rev.* **1995**, *144*, 369−460.
(42) Farrar, J. A.; Neese, F.; Lappalainen, P.; Kroneck, P. M. H.; Saraste, M.; Zumft, W. G.; Thomson, A. J. *J. Am. Chem. Soc.* **1996**, *118*, 11501−11514.
(43) Neese, F.; Solomon, E. I. *J. Am. Chem. Soc.* **1998**, *120*, 12829−12848.
(44) Gamelin, D. R.; Randall, D. W.; Hay, M. T.; Houser, R. P.; Mulder, T. C.; Canters, G. W.; de Vries, S.; Tolman, W. B.; Lu, Y.; Solomon, E. I. *J. Am. Chem. Soc.* **1998**, *120*, 5246−5263.
(45) Paulat, F.; Lehnert, N. *Inorg. Chem.* **2008**, *47*, 4963−4976.
(46) Johansson, F. B.; Bond, A. D.; Nielsen, U. G.; Moubaraki, B.; Murray, K. S.; Berry, K. J.; Larrabee, J. A.; McKenzie, C. J. *Inorg. Chem.* **2008**, *47*, 5079−5092.
(47) Larrabee, J. A.; Johnson, W. R.; Volwiler, A. S. *Inorg. Chem.* **2009**, *48*, 8822−8829.
(48) Gamelin, D. R.; Kirk, M. L.; Stemmler, T. L.; Pal, S.; Armstrong, W. H.; Pennerhahn, J. E.; Solomon, E. I. *J. Am. Chem. Soc.* **1994**, *116*, 2392−2399.
(49) Brunold, T. C.; Gamelin, D. R.; Stemmler, T. L.; Mandal, S. K.; Armstrong, W. H.; Penner-Hahn, J. E.; Solomon, E. I. *J. Am. Chem. Soc.* **1998**, *120*, 8724−8738.
(50) Brunold, T. C.; Gamelin, D. R.; Solomon, E. I. *J. Am. Chem. Soc.* **2000**, *122*, 8511−8523.
(51) Jackson, T. A.; Karapetian, A.; Miller, A. F.; Brunold, T. C. *J. Am. Chem. Soc.* **2004**, *126*, 12477−12491.
(52) Geiger, R. A.; Chattopadhyay, S.; Day, V. W.; Jackson, T. A. *J. Am. Chem. Soc.* **2010**, *132*, 2821−2831.
(53) Chattopadhyay, S.; Geiger, R. A.; Yin, G. C.; Busch, D. H.; Jackson, T. A. *Inorg. Chem.* **2010**, *49*, 7530−7535.
(54) Bane, K.; Geiger, R. A.; Chabolla, S. A.; Jackson, T. A. *Inorg. Chim. Acta* **2012**, *380*, 135−140.
(55) Whittaker, J. W.; Whittaker, M. M. *J. Am. Chem. Soc.* **1991**, *113*, 5528−5540.
(56) Jackson, T. A.; Karapetian, A.; Miller, A. F.; Brunold, T. C. *Biochemistry* **2005**, *44*, 1504−1520.
(57) Woertink, J. S.; Tian, L.; Maiti, D.; Lucas, H. R.; Himes, R. A.; Karlin, K. D.; Neese, F.; Wurtele, C.; Holthausen, M. C.; Bill, E.; Sundermeyer, J.; Schindler, S.; Solomon, E. I. *Inorg. Chem.* **2010**, *49*, 9450−9459.
(58) Stephens, P. J. *J. Chem. Phys.* **1970**, *52*, 3489−3516.
(59) Stephens, P. J. *Annu. Rev. Chem. Phys.* **1974**, *25*, 201−232.

(60) Westphal, A.; Broda, H.; Kurz, P.; Neese, F.; Tuczek, F. *Inorg. Chem.* **2012**, *51*, 5748−5763.
(61) Ganyushin, D.; Neese, F. *J. Chem. Phys.* **2008**, *128*, 114117.
(62) Sundararajan, M.; Ganyushin, D.; Ye, S. F.; Neese, F. *Dalton Trans.* **2009**, 6021−6036.
(63) Peralta, G. A.; Seth, M.; Zhekova, H.; Ziegler, T. *Inorg. Chem.* **2008**, *47*, 4185−4198.
(64) Hernandez-Marin, E.; Seth, M.; Ziegler, T. *Inorg. Chem.* **2010**, *49*, 1566−1576.
(65) Boucher, L. J.; Day, V. W. *Inorg. Chem.* **1977**, *16*, 1360−1367.
(66) McCarthy, P. J.; Hovey, R. J.; Ueno, K.; Martell, A. E. *J. Am. Chem. Soc.* **1955**, *77*, 5820−5824.
(67) Stoll, S.; Schweiger, A. *J. Magn. Reson.* **2006**, *178*, 42−55.
(68) Frisch, M. J.; Trucks, G. W.; Schlegel, H. B.; Scuseria, G. E.; Robb, M. A.; Cheeseman, J. R.; Montgomery, Jr., J. A.; Vreven, T.; Kudin, K. N.; Burant, J. C.; Millam, J. M.; Iyengar, S. S.; Tomasi, J.; Barone, V.; Mennucci, B.; Cossi, M.; Scalmani, G.; Rega, N.; Petersson, G. A.; Nakatsuji, H.; Hada, M.; Ehara, M.; Toyota, K.; Fukuda, R.; Hasegawa, J.; Ishida, M.; Nakajima, T.; Honda, Y.; Kitao, O.; Nakai, H.; Klene, M.; Li, X.; Knox, J. E.; Hratchian, H. P.; Cross, J. B.; Bakken, V.; Adamo, C.; Jaramillo, J.; Gomperts, R.; Stratmann, R. E.; Yazyev, O.; Austin, A. J.; Cammi, R.; Pomelli, C.; Ochterski, J. W.; Ayala, P. Y.; Morokuma, K.; Voth, G. A.; Salvador, P.; Dannenberg, J. J.; Zakrzewski, V. G.; Dapprich, S.; Daniels, A. D.; Strain, M. C.; Farkas, O.; Malick, D. K.; Rabuck, A. D.; Raghavachari, K.; Foresman, J. B.; Ortiz, J. V.; Cui, Q.; Baboul, A. G.; Clifford, S.; Cioslowski, J.; Stefanov, B. B.; Liu, G.; Liashenko, A.; Piskorz, P.; Komaromi, I.; Martin, R. L.; Fox, D. J.; Keith, T.; Al-Laham, M. A.; Peng, C. Y.; Nanayakkara, A.; Challacombe, M.; Gill, P. M. W.; Johnson, B.; Chen, W.; Wong, M. W.; Gonzalez, C.; Pople, J. A. *Gaussian 03*, Revision C.02; Gaussian, Inc.: Wallingford, CT, 2004.
(69) Becke, A. D. *J. Chem. Phys.* **1993**, *98*, 5648−5652.
(70) Lee, C. T.; Yang, W. T.; Parr, R. G. *Phys. Rev. B* **1988**, *37*, 785−789.
(71) Miehlich, B.; Savin, A.; Stoll, H.; Preuss, H. *Chem. Phys. Lett.* **1989**, *157*, 200−206.
(72) Dunning, T. H., Jr.; Hay, P. J. *Modern Theoretical Chemistry*; Schaefer, H. F.; III, Ed.; Plenum: New York, 1976.
(73) Hay, P. J.; Wadt, W. R. *J. Chem. Phys.* **1985**, *82*, 270−283.
(74) Hay, P. J.; Wadt, W. R. *J. Chem. Phys.* **1985**, *82*, 299−310.
(75) Wadt, W. R.; Hay, P. J. *J. Chem. Phys.* **1985**, *82*, 284−298.
(76) Weigend, F.; Ahlrichs, R. *Phys. Chem. Chem. Phys.* **2005**, *7*, 3297−3305.
(77) Feller, D. *J. Comput. Chem.* **1996**, *17*, 1571−1586.
(78) Schuchardt, K. L.; Didier, B. T.; Elsethagen, T.; Sun, L. S.; Gurumoorthi, V.; Chase, J.; Li, J.; Windus, T. L. *J. Chem. Inf. Model.* **2007**, *47*, 1045−1052.
(79) Allouche, A. R. *J. Comput. Chem.* **2011**, *32*, 174−182.
(80) Hendrich, M. P.; Debrunner, P. G. *Biophys. J.* **1989**, *56*, 489−506.
(81) Miyasaka, H.; Clerac, R.; Ishii, T.; Chang, H. C.; Kitagawa, S.; Yamashita, M. *J. Chem. Soc., Dalton Trans.* **2002**, 1528−1534.
(82) Biswas, S.; Mitra, K.; Adhikary, B.; Lucas, C. R. *Trans. Met. Chem.* **2005**, *30*, 586−592.
(83) Bhowmik, P.; Nayek, H. P.; Corbella, M.; Aliaga-Alcalde, N.; Chattopadhyay, S. *Dalton Trans.* **2011**, *40*, 7916−7926.
(84) Carducci, M. D.; Brown, C.; Solomon, E. I.; Enemark, J. H. *J. Am. Chem. Soc.* **1994**, *116*, 11856−11868.
(85) Neese, F. Ph.D. Thesis, Universität Konstanz, Konstanz, Baden-Württemberg, Germany, 1997.